Finally, before performing the design operations to curve the piece, it must be validated that the bed satisfies the bijectivity between World space and Slicing space across the entire domain of the piece. Figure 6.12 demonstrates that, in this case, since the bed is fully convex, this property is upheld, allowing the piece to be transformed without any impediments. The blue lines in the figure represent the normal at each point on the surface. Since they never intersect, there is only one normal to the surface that can reach each point in space, thus satisfying the bijectivity condition.

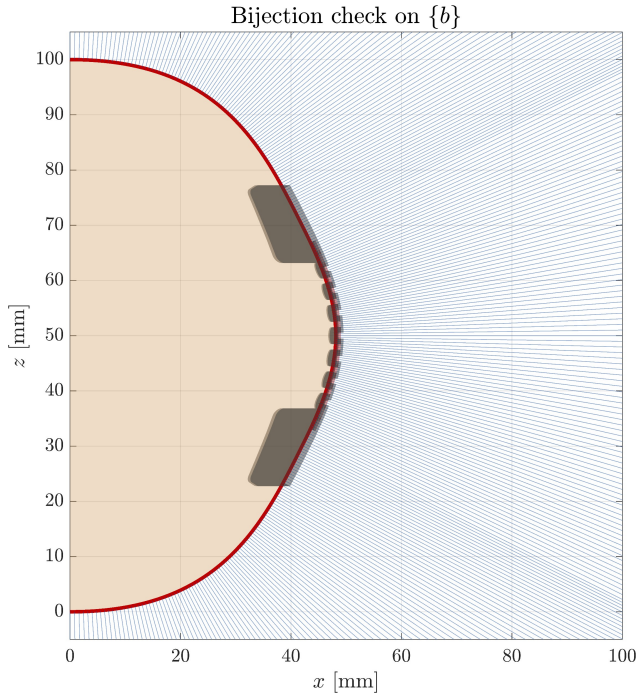

Figure 6.12: Bijection check of the designed part on the selected build platform.

Figure 6.13 illustrates how, starting from the original CAD design of a part, it can be scaled using the spline data to a format that meets the required specifications once designed with curvature and avoids excessive deformation. Once the space $\{e\}$ has been defined, the necessary adjustments need to be made for the part to fit in the defined space. After the transformation, the final result shows how the part fits in the designed space and shares its curvature where the future building layers will be generated.

6.1.5 Non planar slicing process for DfNPAM actuators

Once the STL files for the actuators have been generated as output from the DfNPAM process, they are then sliced to obtain the print paths. In this case, given a dual-material design, we will use Ultimaker CURA's bypass mode, as it computes more quickly but complicates the part placement process and does not optimize layer infill.

Since the part has already been designed and scaled in $\{e\}$, as shown in Figure 6.13.c, the file is sent directly to CURA, where the paths for both bodies, PETG and PVA, are generated. Once the paths are created, they are parsed to interpolate points along the paths, then

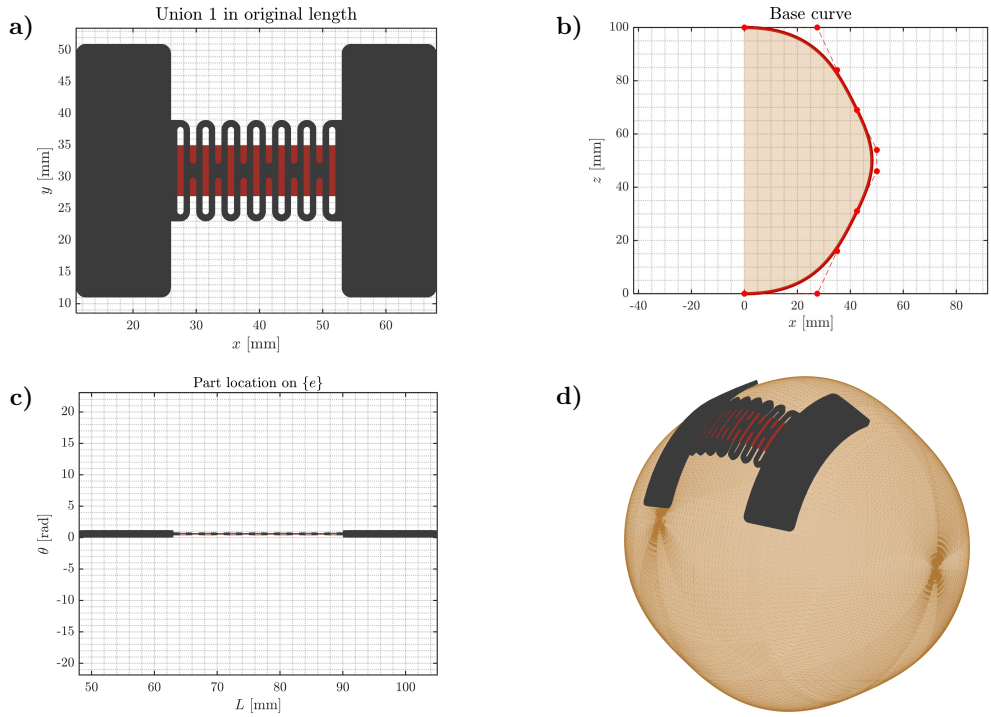

Figure 6.13: Design process. a) Original part in $\{b\}$. b) build platform used to define $\{e\}$. c) Deformed and located part to fit in $\{e\}$. d) Final design result in $\{b\}$

transformed to $\{b\}$ and exported for robotic execution. Figure 6.14 illustrates the operation of the slicer when starting from an object previously designed for NPAM. Here, the first module of the program is bypassed since the model is already scaled in $\{e\}$.

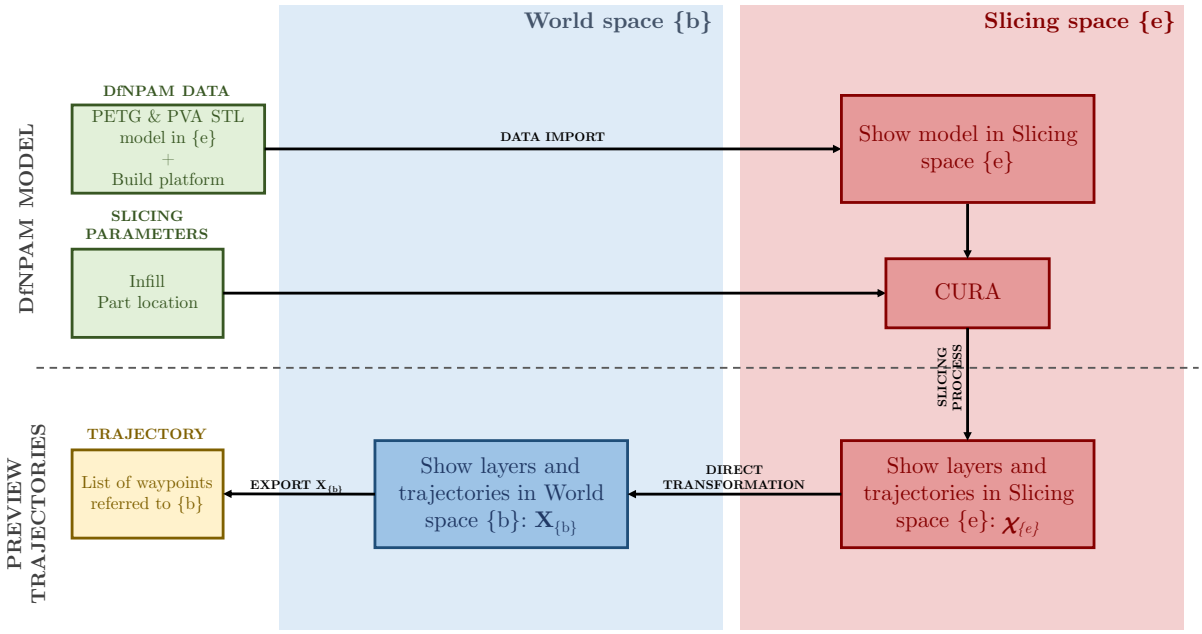

Figure 6.14: Slicing operations when parts have been already designed for NPAM.

Finally, the necessary homogeneous transformation is applied to the trajectories to reference them to the print bed frame on which they will be executed, and they are then exported.

6.2 Results and Discussion

6.2.1 Planar resting state origami actuators library

Once the origami patterns were designed, printed, and evaluated, and after conducting simulations and experimental tests, the results obtained at each phase of the research are presented and analyzed. Subsequently, these results are discussed in relation to the initial objectives, highlighting the key findings derived from the study.

Design and printing of origami patterns

First, the results stemming from the application of design principles and criteria to the selected origami patterns are presented. Each pattern was assigned the values for the parameters defined in section 6.1.3. The origami patterns were designed for all types of folding zones considered, with a length of $21mm - 27mm$. The figures generated from the design tool, showing the results from both the design and fabrication phases, are presented below.

For the design of folding zone 2, which is subdivided into three options, only the image for option 2.1 is shown since the visual appearance of the three options is quite similar. The designs have been optimized for material usage, mainly by adding through-holes in the facets. Furthermore, all the origami patterns developed in the library share the same morphology, rounded corners, and the presence of holes, ensuring coherence. The design library is organized and labeled according to pattern types and the folding zones they contain. These results demonstrate the creation of a comprehensive and diverse library, featuring both classical and modified origami patterns.

Figures 6.15-6.19 show the complete library of printed patterns and their associated designs.

Dynamic simulation of folding zones

After conducting the finite element analysis of the folding zones, the following results were obtained. The results show the comparison between modeled folding zones with different lengths, 21, 24, and $27mm$, for the values of maximum principal stress, equivalent elastic strain.

- **Folding zone 1:** Figure 6.20 presents the results of the FEM analysis conducted on folding zone 1 with a length of $27mm$. Table 6.3 presents the results for the three evaluated lengths of applied force up to the yield of PVA, maximum principal stress, equivalent elastic strain, and maximum principal strain, compared with the yield stress of each material comprising the folding zone.

  Although the applied force is slightly lower in the longer folding zones (L24 and L27), this small variation is related to the distribution of the load over a greater length. The longer folding zones distribute the force more efficiently, which could explain the reduction in the force required to achieve the same levels of deformation and stress.

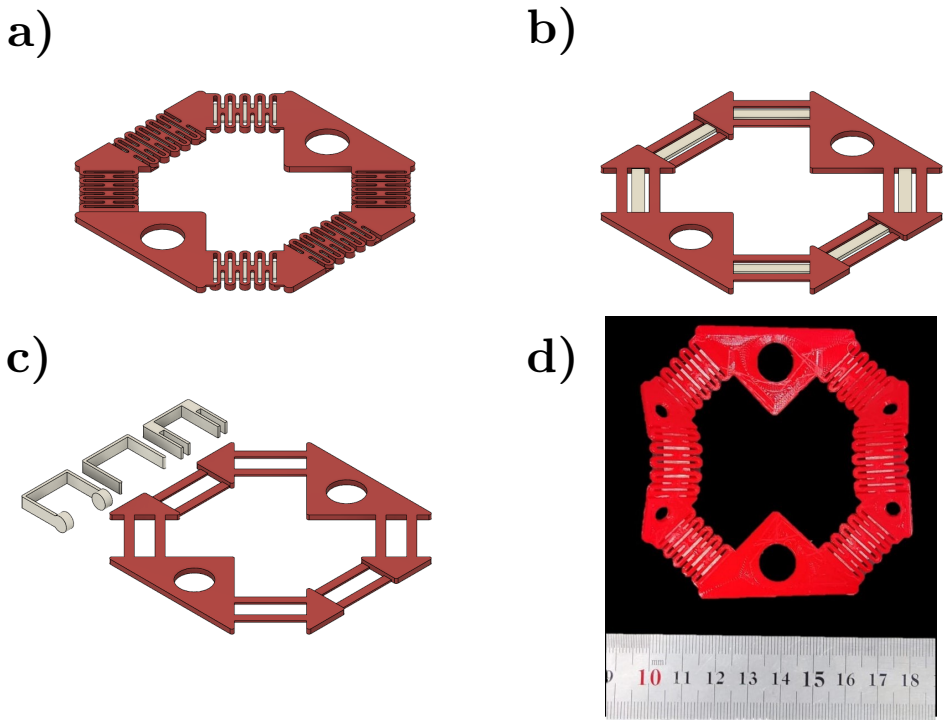

Figure 6.15: Yoshimura pattern design and fabrication results. a) Folding zone 1. b) Folding zone 2.1. c) Folding zone 3. d) Manufactured Yoshimura pattern with folding zone 1.

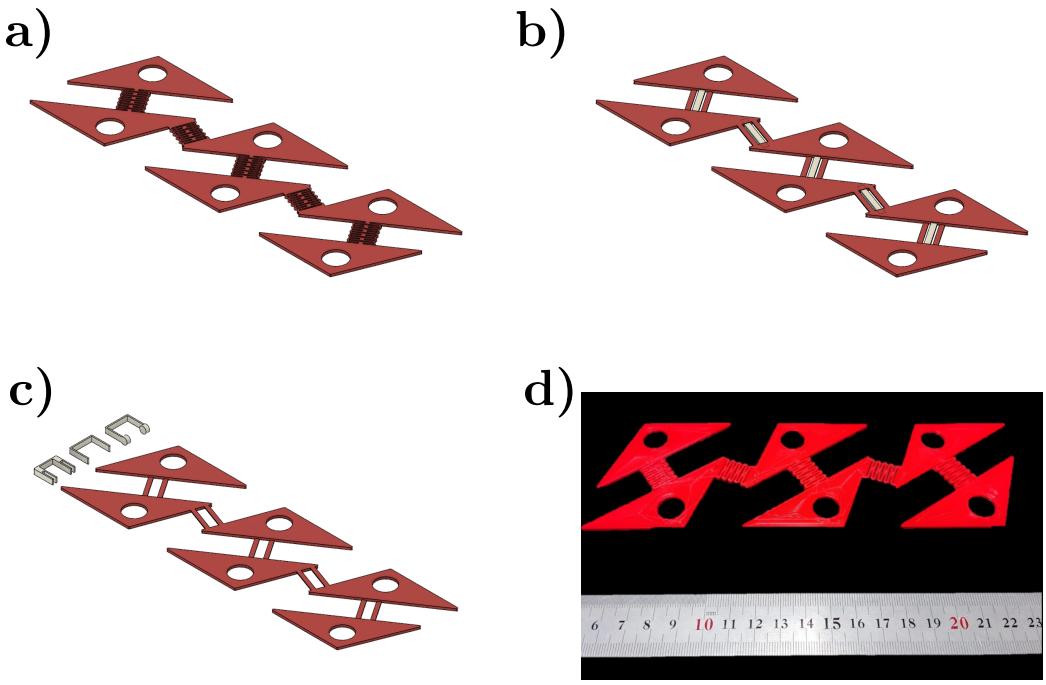

Figure 6.16: Kresling pattern design and fabrication results. a) Folding zone 1. b) Folding zone 2.1. c) Folding zone 3. d) Manufactured Kresling pattern with folding zone 1.

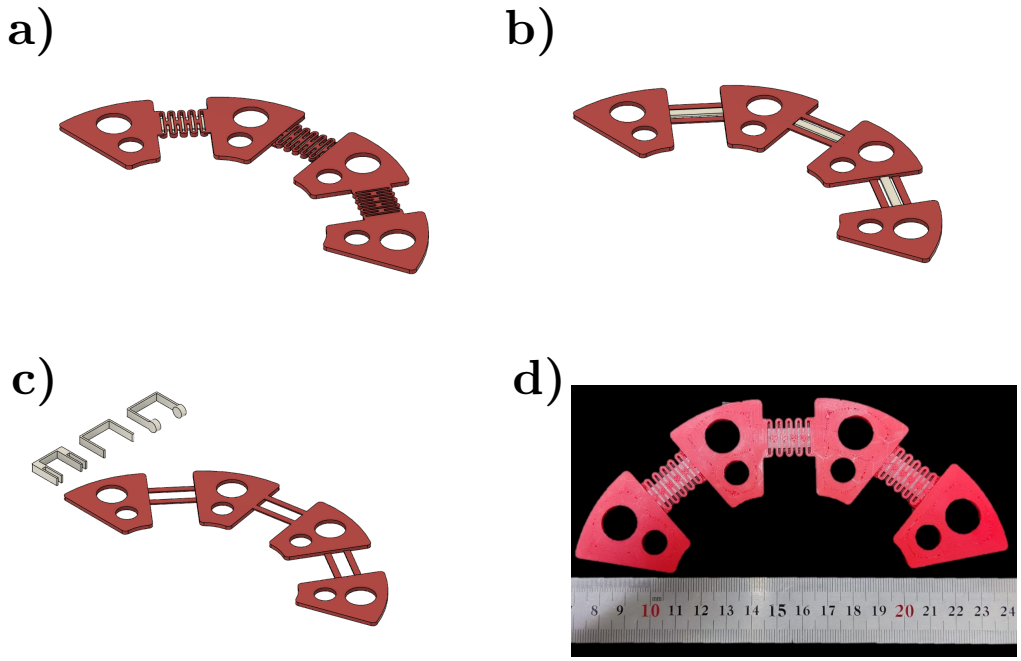

Figure 6.17: Accordion fan pattern design and fabrication results. a) Folding zone 1. b) Folding zone 2.1. c) Folding zone 3. d) Manufactured Accordion Fan pattern with folding zone 1.

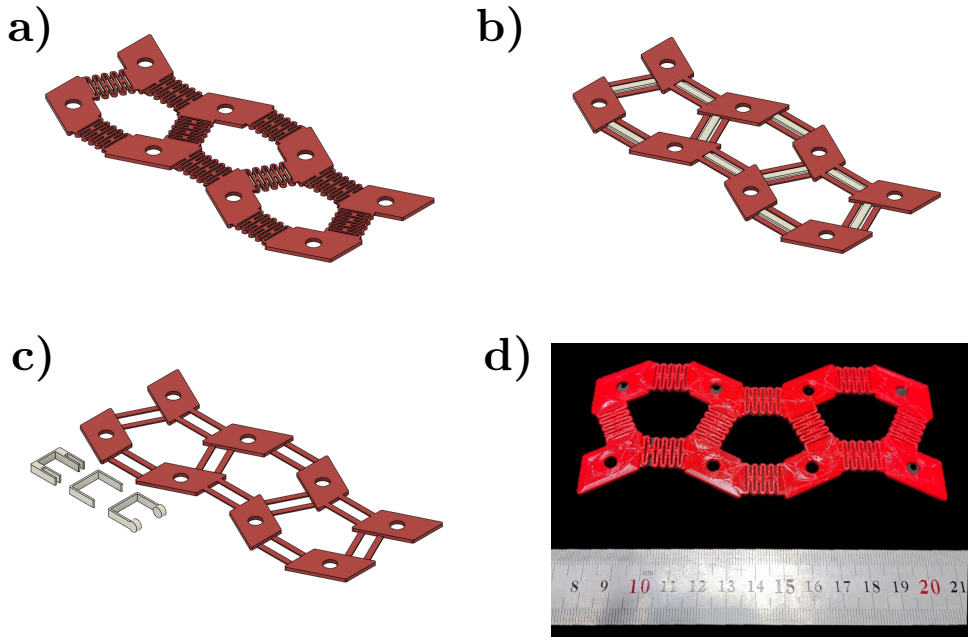

Figure 6.18: Miura-ori pattern design and fabrication results. a) Folding zone 1. b) Folding zone 2.1. c) Folding zone 3. d) Manufactured Miura-ori pattern with folding zone 1.

The equivalent elastic strain remains practically constant despite the differences in the length of the folding zones. This suggests that, regardless of the length, the material

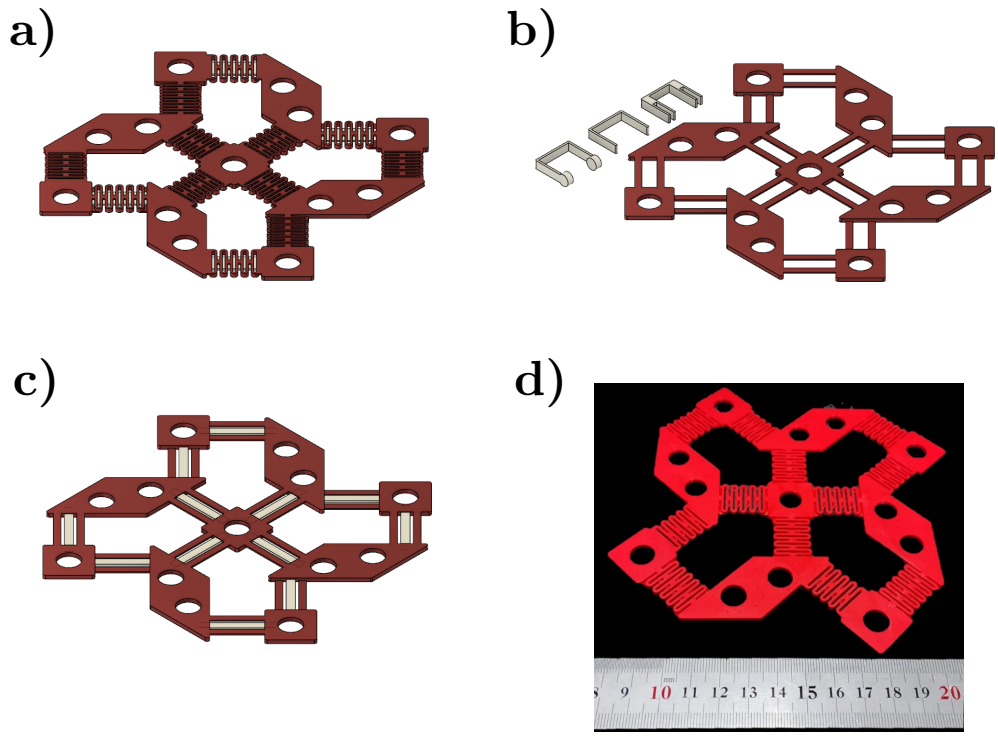

Figure 6.19: Square Twist pattern design and fabrication results. a) Folding zone 1. b) Folding zone 2.1. c) Folding zone 3. d) Manufactured Square Twist pattern with folding zone 1.

responds uniformly in terms of elasticity under the applied load conditions.

The slight trend toward an increase in maximum principal strain as the folding zone length increases may indicate that longer folding zones experience a higher degree of stress concentration at their most critical points. While longer folding zones require less force to reach the same deformation, they may be subject to more critical material behavior at stress concentration points.

The maximum stress in the PVA remains stable across all three folding zones. This suggests that, regardless of the folding zone length, the PVA material responds similarly to the applied loads. Furthermore, its value remains in the range of interest, being higher than the yield stress (22 MPa) but lower than the UTS (78 MPa).

The decrease in maximum stress in PETG as the folding zone length increases suggests that the longer folding zones may distribute stresses better, reducing the maximum load experienced by the material. This is a positive outcome, as lower stress reduces the likelihood of reaching PETG's yield point, thereby lowering the risk of permanent deformations.

- **Folding zone 2.1:** Figure 6.21 displays the findings from the FEM analysis performed on folding zone 2.1, which measures $24mm$. In addition, Table 6.4 outlines the results for three assessed lengths of applied force leading to the yield of PVA, along with maximum principal stress, equivalent elastic strain, and maximum principal strain, all compared

Table 6.3: Simulation results for the three evaluated lengths of folding zone 1: applied force up to the yield of PVA, maximum principal stress, equivalent elastic strain, and maximum principal strain

Parameter	$L = 21mm$	$L = 24mm$	$L = 27mm$
Force at PVA's UTS	$36N$	$35.3N$	$35N$
Equivalent elastic strain	4.34%	4.33%	4.33%
Maximum principal strain	3.21%	3.27%	3.33%
Maximum stress (PVA)	$77.96MPa$	$77.99MPa$	$77.97MPa$
Maximum stress (PETG)	$43.94MPa$	$43.75MPa$	$42.42MPa$

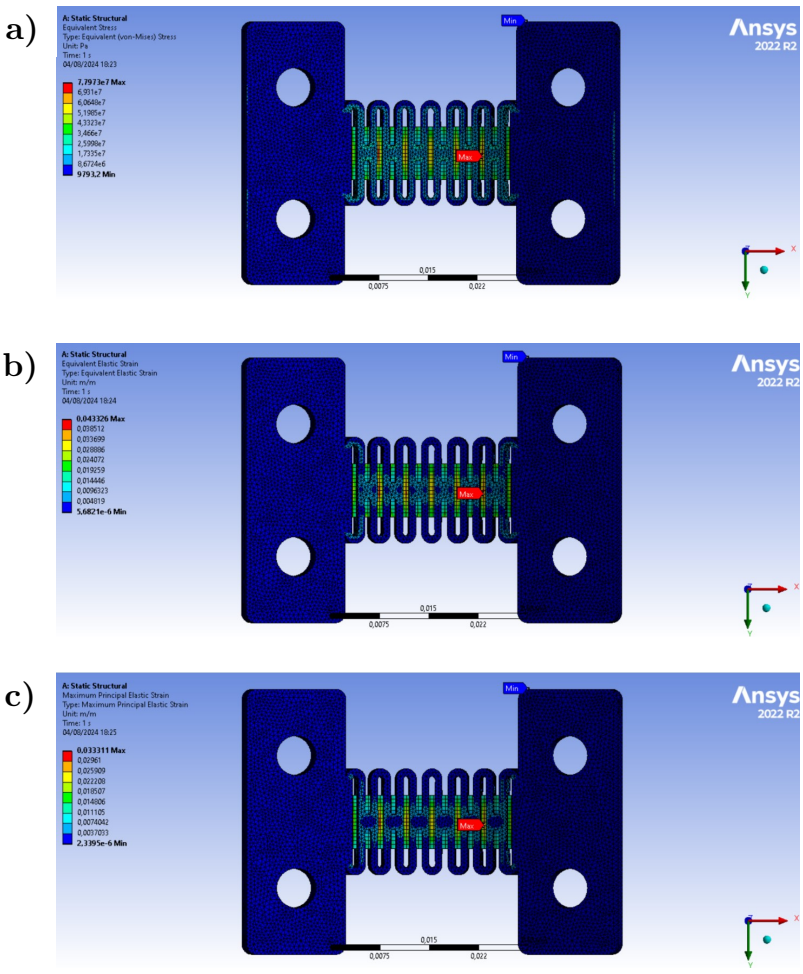

Figure 6.20: FEM analysis of folding zone 1 with $27mm$ length.a)Equivalent stress. b) Equivalent elastic strain. c) Maximum principal elastic strain.

against the yield stress of the materials constituting the folding zone.

Similar to the previous analysis, the applied force shows a slight decrease with an increase in the length of the folding zone. This may be attributed to a more effective load distribution in the longer folding zones, resulting in a slight reduction in the force required to achieve the same deformation conditions.

The equivalent elastic strain is remarkably consistent across all folding zones, exhibiting a slight yet virtually insignificant variation. This suggests that, in terms of elasticity, the material responds uniformly regardless of the folding zone length.

In contrast to the previous case, there is a slight decrease in the maximum principal strain as the length of the folding zone increases. This indicates that, in longer folding zones, the concentration of stresses is lower, thereby reducing deformation at critical points.

The maximum stresses in PVA remain relatively constant, with minimal changes observed. This behavior suggests that PVA maintains its structural integrity irrespective of the folding zone length. Moreover, in all three cases, the maximum stress values remain within the relevant ranges, specifically above the yield stress (22 MPa) but below the ultimate tensile strength (78 MPa).

Conversely, the maximum stress in PETG exhibits a slight decrease as the length of the folding zone increases, paralleling the observations made with PVA. This reduction implies that longer folding zones distribute stresses more efficiently.

Table 6.4: Simulation results for the three evaluated lengths of folding zone 2.1: applied force up to the yield of PVA, maximum principal stress, equivalent elastic strain, and maximum principal strain

Parameter	$L = 21mm$	$L = 24mm$	$L = 27mm$
Force at PVA's UTS	$49.3N$	$49.1N$	$48.6N$
Equivalent elastic strain	4.36%	4.37%	4.37%
Maximum principal strain	2.47%	2.43%	2.43%
Maximum stress (PVA)	$77.92MPa$	$77.98MPa$	$77.84MPa$
Maximum stress (PETG)	$55.97MPa$	$54.34MPa$	$54.73MPa$

- **Folding zone 2.2:** Figure 6.22 illustrates the results obtained from the FEM analysis conducted on folding zone 2.2, measuring $24mm$. Additionally, Table 6.5 summarizes the outcomes for three evaluated lengths of applied force that result in the yield of PETG, as well as the maximum principal stress, equivalent elastic strain, and maximum principal strain, all contrasted with the yield stress of the materials that make up the folding zone.

  In this scenario, the applied force remains consistent across all three folding zones, indicating that the length of the folding zone does not influence the amount of force needed to achieve the observed deformation and stress conditions in the material.

  A slight variation is noted in the equivalent elastic strain for folding zone 2.2 (L24), which is marginally higher than that in the L21 and L27 zones; however, this difference is minimal and not statistically significant.

  The maximum principal elastic strain is nearly identical across all folding zones, with only a slight decrease observed in the L27 zone. This suggests a uniform material behavior, devoid of significant critical stress concentrations.

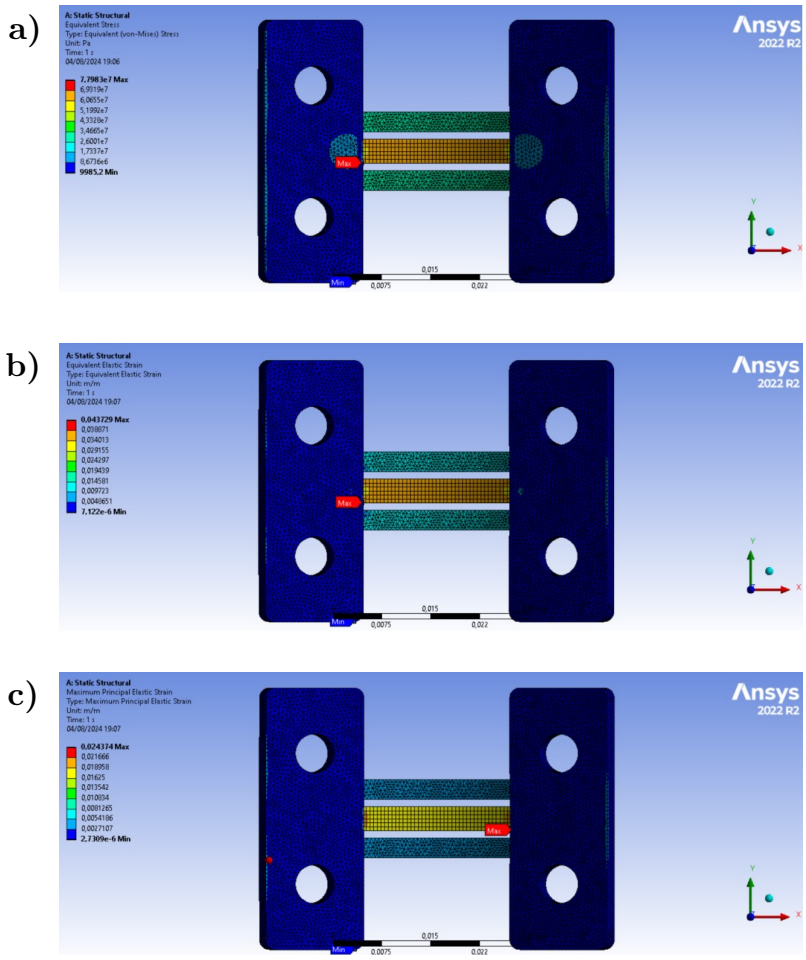

Figure 6.21: FEM analysis of folding zone 2.1 with 24mm length.a)Equivalent stress. b) Equivalent elastic strain. c) Maximum principal elastic strain.

The maximum stress in PVA shows a slight decrease in folding zone 2.2 (L24) compared to the other two zones, but this variation is minimal and appears to have no substantial impact. Notably, for this folding zone, the PVA remains at a maximum stress significantly lower than its ultimate tensile strength (UTS), primarily due to the earlier onset of plastic deformation in PETG, which is an unfavorable condition.

The maximum stresses in PETG are quite similar across all folding zones, with slight differences that do not suggest any clear trend. This indicates that PETG responds uniformly to the applied force across all folding zone lengths. However, unlike in the previous folding zones, there is a situation where PETG begins to plastify before PVA approaches its UTS, which is an undesirable behavior.

- **Folding zone 2.3:** Figure 6.23 presents the findings from the FEM analysis carried out on folding zone 2.3, which has a length of 24mm. Furthermore, Table 6.6 compiles the results for three assessed lengths of applied force leading to the yielding of PETG, alongside the maximum principal stress, equivalent elastic strain, and maximum principal strain, all compared to the yield stress of the materials constituting the folding zone.

Table 6.5: Simulation results for the three evaluated lengths of folding zone 2.2: applied force up to the yield of PETG, maximum principal stress, equivalent elastic strain, and maximum principal strain

Parameter	$L = 21mm$	$L = 24mm$	$L = 27mm$
Force at PVA's UTS	$15.4N$	$15.4N$	$15.4N$
Equivalent elastic strain	1.97%	2.03%	1.97%
Maximum principal strain	1.95%	1.95%	1.94%
Maximum stress (PVA)	$32.99MPa$	$32.39MPa$	$32.95MPa$
Maximum stress (PETG)	$57.71MPa$	$57.58MPa$	$57.62MPa$

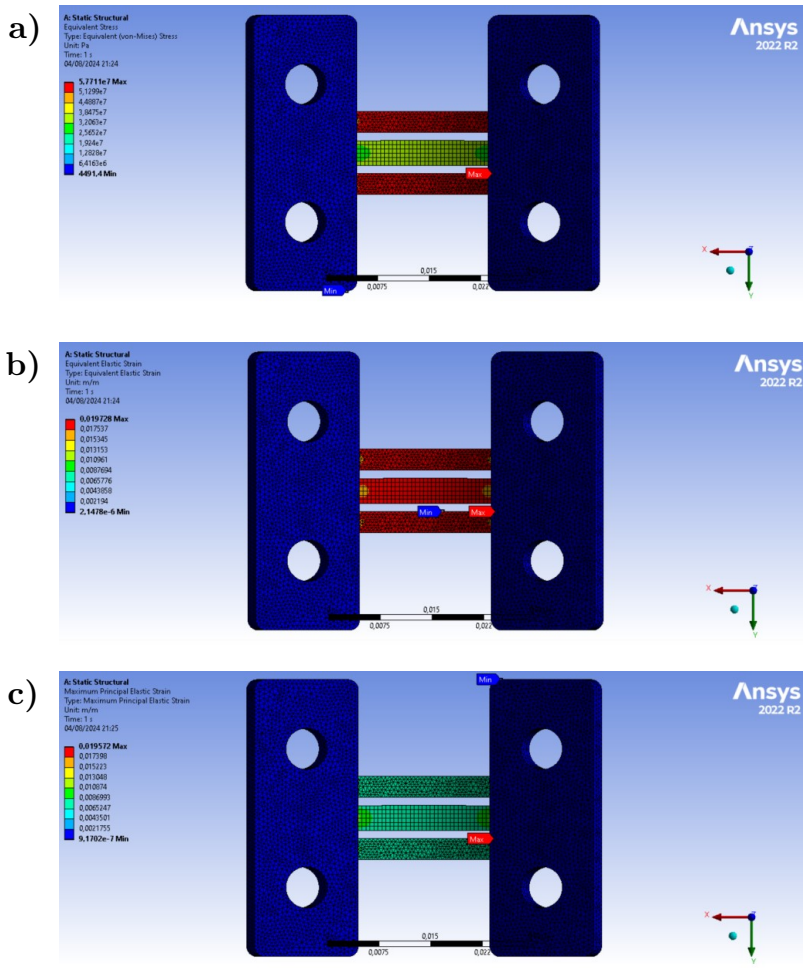

Figure 6.22: FEM analysis of folding zone 2.2 with $21mm$ length.a)Equivalent stress. b) Equivalent elastic strain. c) Maximum principal elastic strain.

Overall, the behavior of this folding zone is rather unpredictable and does not exhibit clear trends, unlike the previous four zones. This may be attributed to the fact that the thickness of the PVA is the same as that of the PETG in the folding zone.

The applied force shows a slight increase with the folding zone length up to 24 mm,

followed by a minor decrease at $27mm$. This may suggest that longer folding zones can distribute the load more efficiently; however, there could also be additional factors influencing the applied force.

The equivalent elastic strain exhibits a small increase in the 24 mm folding zone and a slight decrease in the $27mm$ zone. The greater strain in the L24 zone could result from a higher concentration of stresses at that intermediate length, while the reduction in L27 may reflect improved load distribution in the longer folding zone.

The maximum principal strain remains quite consistent, with a slight upward trend observed in the $27mm$ folding zone. This could indicate that, despite the overall improvement in stress distribution within the longer folding zones, there exists a stress concentration point leading to greater deformation in the longest zone.

The maximum stress in PVA increases in the L24 folding zone, followed by a slight decrease in the L27 zone. This may suggest that the length of the folding zone affects stress distribution, with the intermediate zone experiencing a higher maximum stress. Conversely, it is noteworthy that in this folding zone, the PVA maintains a maximum stress significantly lower than its UTS, as the PETG initiates yielding beforehand, which is an unfavorable outcome.

Maximum stresses in PETG increase slightly with the length of the folding zone, indicating that longer folding zones are subjected to greater stresses in the PETG. This trend suggests a potential point at which the length of the folding zone negatively impacts the maximum stress in PETG, bringing it closer to the yield limit. However, similar to the previous folding zone, it is observed that the PETG yields before the PVA approaches its UTS, which is an undesirable behavior.

Table 6.6: Simulation results for the three evaluated lengths of folding zone 2.3: applied force up to the yield of PETG, maximum principal stress, equivalent elastic strain, and maximum principal strain

Parameter	$L = 21mm$	$L = 24mm$	$L = 27mm$
Force at PVA's UTS	$20.8N$	$21.3N$	$21N$
Equivalent elastic strain	2.73%	2.79%	2.74%
Maximum principal strain	1.95%	1.95%	1.96%
Maximum stress (PVA)	$46.92MPa$	$47.98MPa$	$47.28MPa$
Maximum stress (PETG)	$57.74MPa$	$57.75MPa$	$57.88MPa$

The four studied folding zones (folding zones 1, 2.1, 2.2, and 2.3) have exhibited variations in performance, allowing for a detailed evaluation of how length and specific characteristics influence the behavior of the folding zones under load. The fifth folding zone, folding zone 3, has not been simulated, as its activation mechanism does not rely on the yield strength of the materials that constitute it. Instead, its actuation has been tested directly in water.

The applied forces differed significantly among the folding zones, generally decreasing as the length of the folding zone increased. This downward trend persists across all zones, except for zone 2.3, which demonstrates more unpredictable behavior. This inconsistency may arise

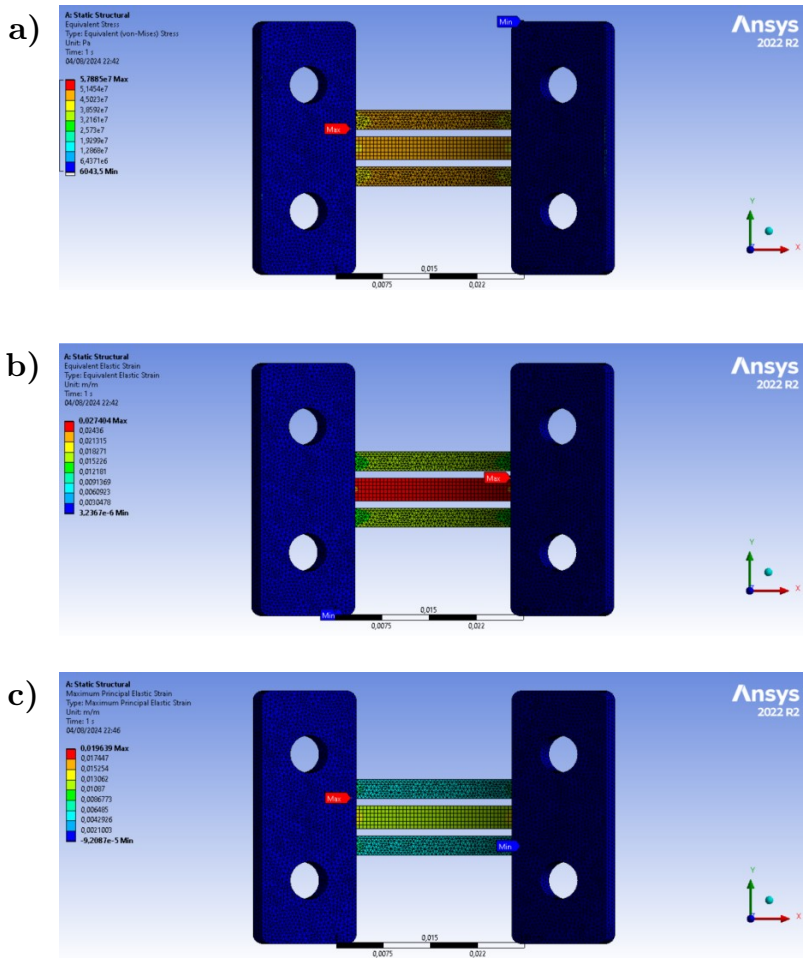

Figure 6.23: FEM analysis of folding zone 2.3 with 27mm length.a)Equivalent stress. b) Equivalent elastic strain. c) Maximum principal elastic strain.

from zone 2.3 having the same thickness of PVA material as PETG, leading to more variable results. Folding zones 1 and 2.1 require a greater applied force to reach the ultimate tensile strength of the PVA material, categorizing them as the most robust zones with lower risks of exceeding the point of structural failure.

The length of the folding zone appears to affect the distribution of strain, with intermediate lengths sometimes showing greater deformations. The maximum principal strain tends to be consistent, with slight variations between lengths for the folding zones 2. In contrast, for folding zone 1, there is an increase with length, suggesting that longer zones may be subjected to greater stress concentrations.

The maximum stress in PVA is generally constant within the same folding zone, regardless of length. However, it is noteworthy that there are differences in values among the zones. Zones 1 and 2.1 are characterized by scenarios where the PVA fails before the PETG begins to plastify, thus accommodating higher stresses in the PVA. In contrast, zones 2.2 and 2.3 are characterized by scenarios where the PETG yields before the PVA fails, limiting the stress values to the point where the PETG starts to plastify. The maximum stresses in PETG are

typically constant for the same folding zone, but once again, the significant differences in maximum stress values according to the considered folding zone are emphasized.

Finally, from a purely dynamic perspective, folding zone 2.1 demonstrates the best performance, particularly at a length of $24mm$. However, folding zone 1 also shows promising behavior, albeit with the drawback of sustaining less force to reach PVA failure and exhibiting a generally higher concentration of stresses.

6.2.2 Non-planar resting state origami actuators library

Based on the library of actuators with a planar resting state, an additional origami actuator library has been developed using the described methodology, with a curved resting state. In this case, the actuators are activated by flattening them, while they curve as the plastically deformed material degrades.

This library has aimed to tailor each shape to a specific fold pattern that enhances its natural deformation. Initially, the folding zones were tested on various print beds. Figures 6.24, 6.25 and 6.26 complement the already described Figure 6.13, displaying joints 1 and 2 on beds with single and double curvature. Folding zone 3 is omitted due to its similarity to zone 2 and simpler structure.

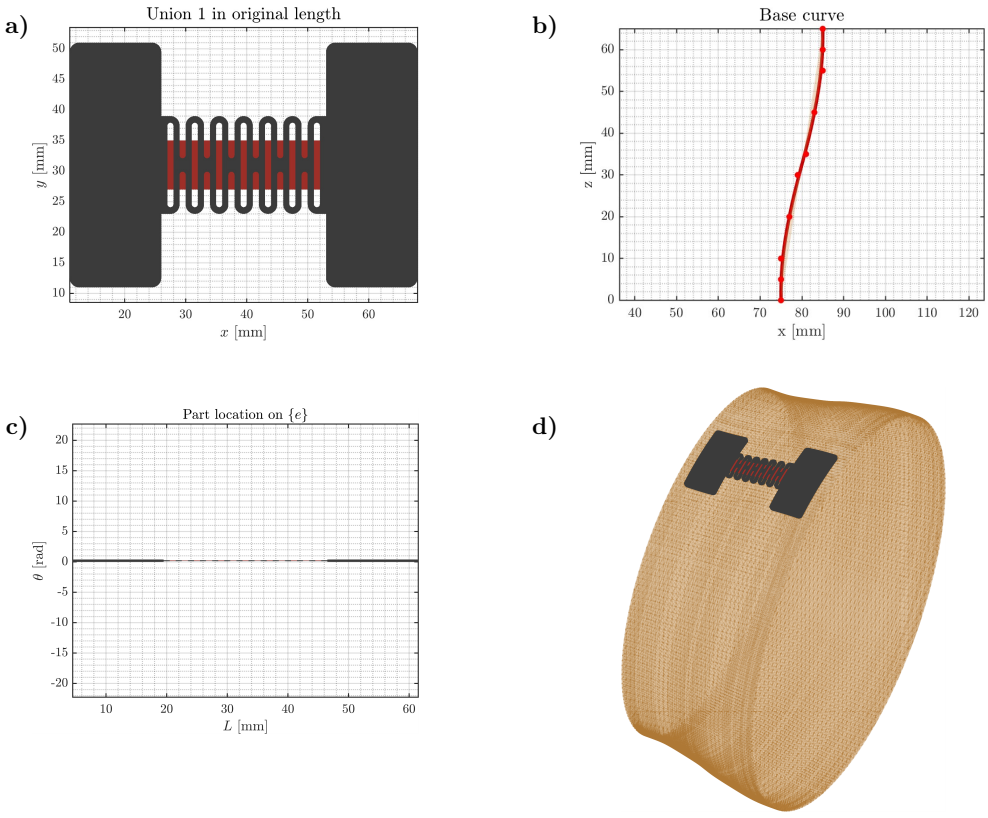

Figure 6.24: Design process of Folding Zone 1 with double curvature. a) Original part in $\{b\}$. b) Build platform used to define $\{e\}$. c) Deformed and located part to fit in $\{e\}$. d) Final design result in $\{b\}$

The main outcome of these initial designs confirms the proposed design theory. Although the original pattern defined in the slicing space $\{e\}$ deforms when adapted to the surface, this deformation can be controlled relatively easily by specifying the theta angle spanned by the entire piece. Additionally, the program itself centers the piece at the L coordinate, allowing different centering points aside from the bed's midpoint. This flexibility offers a variety of design possibilities, enabling the system to adapt to different geometries approximated from the base curve.

For flatter shapes, the base curve can simply be offset from the $z-$axis. Doing so results in shapes that exhibit minimal deformation in the $\theta-$direction. As shown in Figures 6.13 and 6.25, the deformation is significantly greater in theta compared to Figures 6.24 and 6.26.

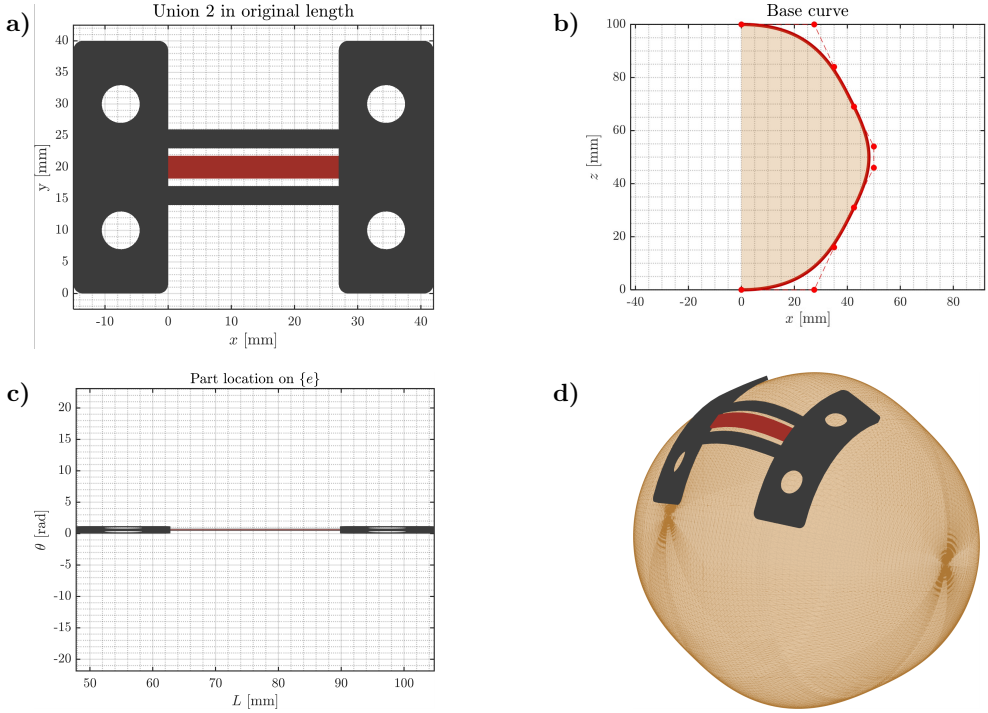

Figure 6.25: Design process of Folding Zone 2 with single curvature. a) Original part in $\{b\}$. b) Build platform used to define $\{e\}$. c) Deformed and located part to fit in $\{e\}$. d) Final design result in $\{b\}$

This design versatility also led to the definition of a folding zone misaligned with the L and $\theta-$design axes in Slicing Space $\{e\}$. The outcome of this validation on a cylindrical bed can be observed in Figure 6.27, which demonstrates how the originally flat piece adapts to this double curvature.

Once the methodology was validated on each Folding Zone type, they were interconnected to replicate origami patterns. All complex structures have been validated using Folding zone 1, as it is the most complex type. This process began with the simplest pattern, a linear connection of folding zones, which already yielded interesting results. Figures 6.28 and 6.29 show the outcome. Using these patterns, a transition from a plane to a cone shape or from a plane to linear compression can be achieved.

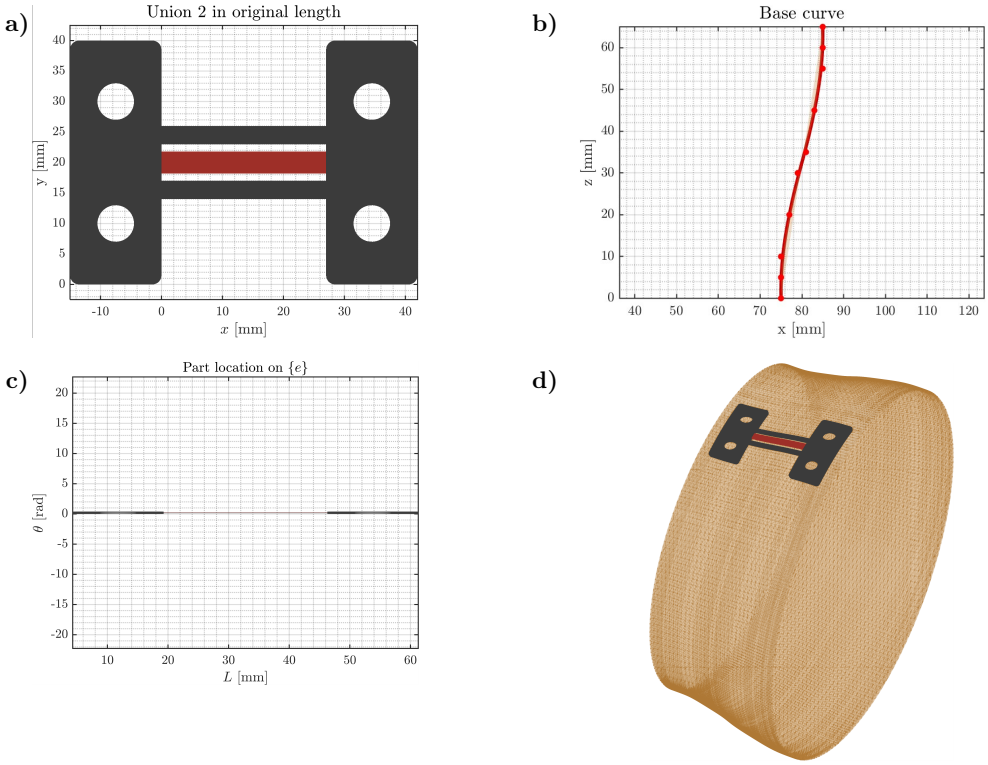

Figure 6.26: Design process of Folding Zone 2 with double curvature. a) Original part in $\{b\}$. b) Build platform used to define $\{e\}$. c) Deformed and located part to fit in $\{e\}$. d) Final design result in $\{b\}$

The designs proposed so far have been successfully transformed in under one minute for the folding zones and within three minutes for the more complex Accordion fan-type patterns.

The results presentation continues with the more complex patterns. In this case, Figures 6.30 through 6.33 illustrate the adaptation of the Yoshimura, Kresling, Square Twist, and Miura Ori patterns to DfNPAM.

All three patterns have been adapted to a spherical curvature, as the goal of this study within the BIOMET4D project was to design skin expanders using NPAM. Additionally, the Miura Ori pattern has been adapted to a double-curved bed for potential use in other applications.

All these mechanisms would function by deforming to a flat state from which they would then take on the spherical shape in which they were printed. Figure 6.34 displays the previously designed patterns on their respective print beds to visualize the printing process.

The DfNPAM process enables the actuator to function as a skin expander, and by using different build platforms, it can be fully tailored to meet the specific requirements of each case.

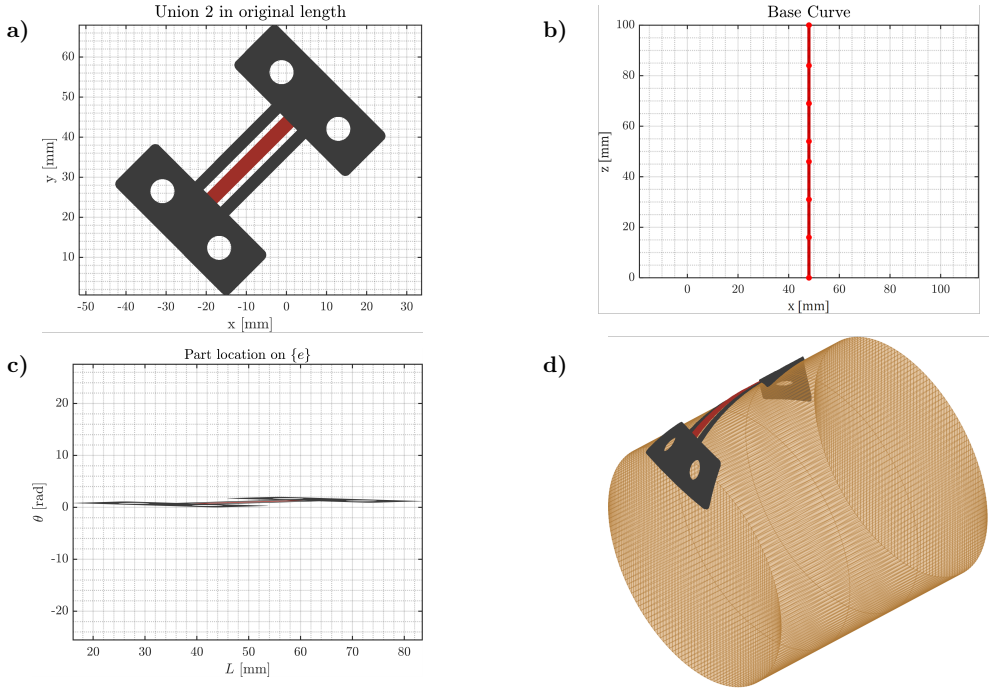

Figure 6.27: Design process of Folding Zone 2 with axis misalignment. a) Original part in $\{b\}$. b) Build platform used to define $\{e\}$. c) Deformed and located part to fit in $\{e\}$. d) Final design result in $\{b\}$

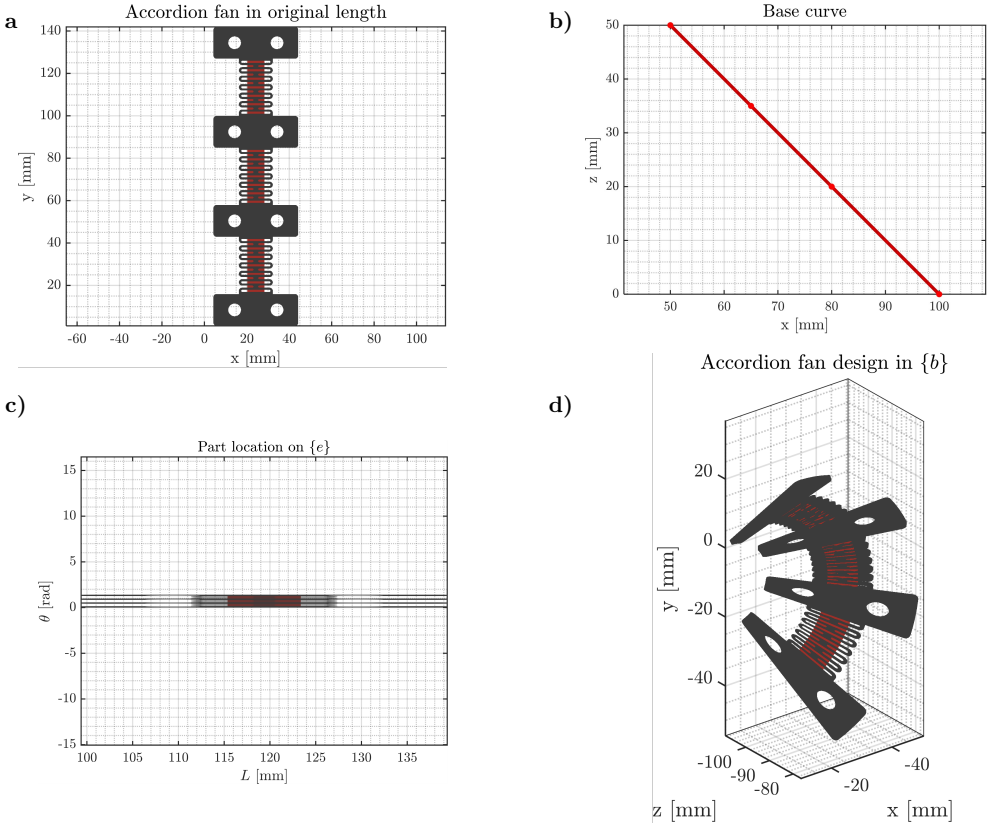

Figure 6.28: Design process of an Accordion Fan on a conical build platform. a) Original part in $\{b\}$. b) Build platform used to define $\{e\}$. c) Deformed and located part to fit in $\{e\}$. d) Final design result in $\{b\}$

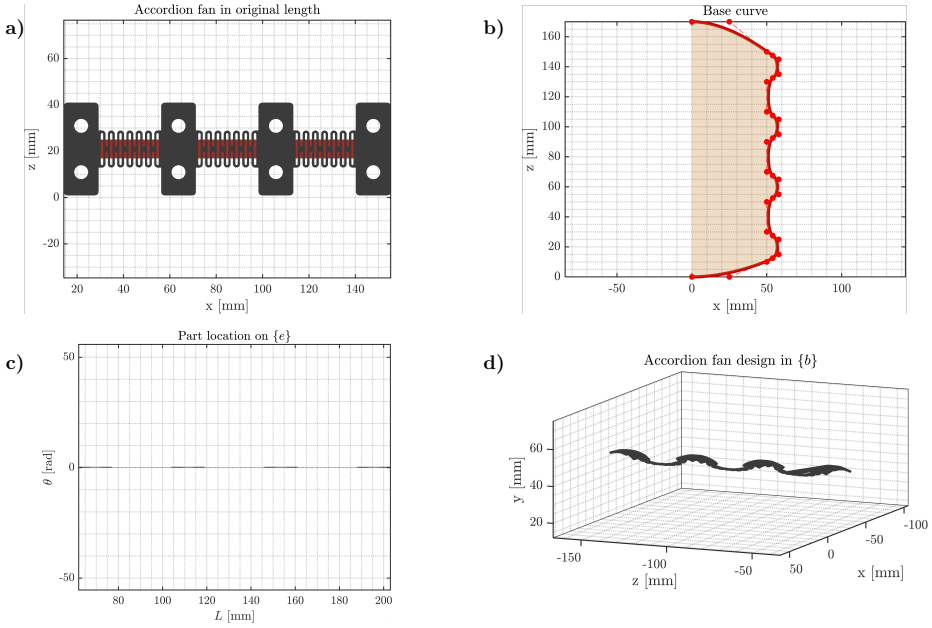

Figure 6.29: Design process of an Accordion Fan on a spring-shaped bed. a) Original part in $\{b\}$. b) Build platform used to define $\{e\}$. c) Deformed and located part to fit in $\{e\}$. d) Final design result in $\{b\}$

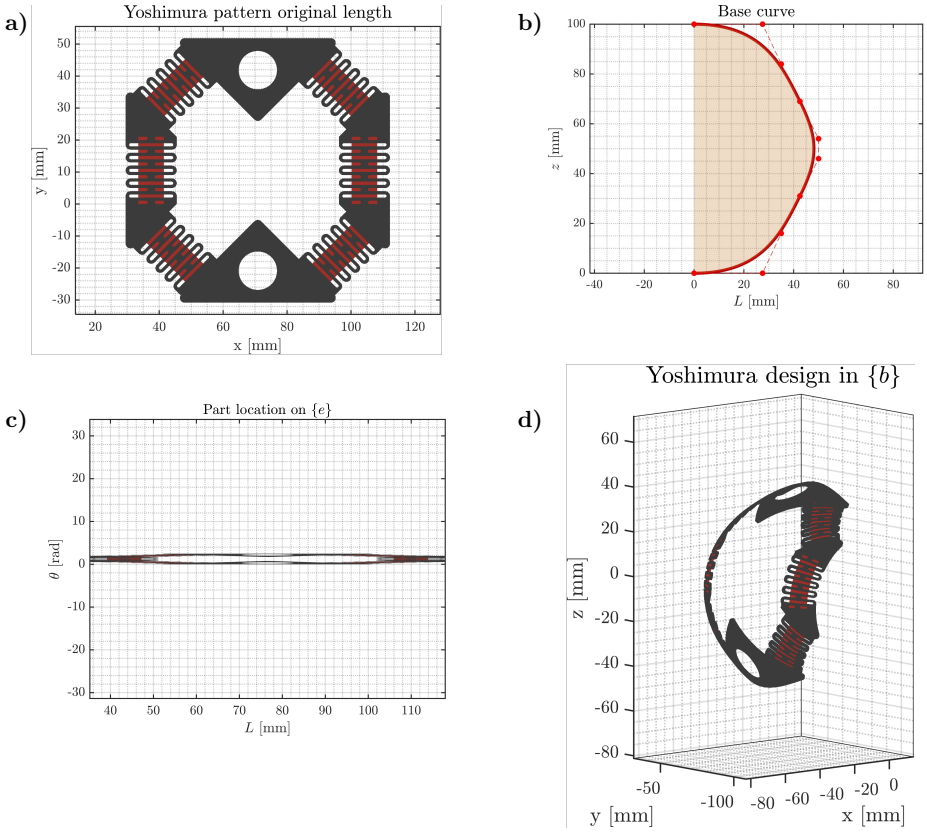

Figure 6.30: Design process of a Yoshimura pattern on a Hollow-shaped build platform. a) Original part in $\{b\}$. b) Build platform used to define $\{e\}$. c) Deformed and located part to fit in $\{e\}$. d) Final design result in $\{b\}$

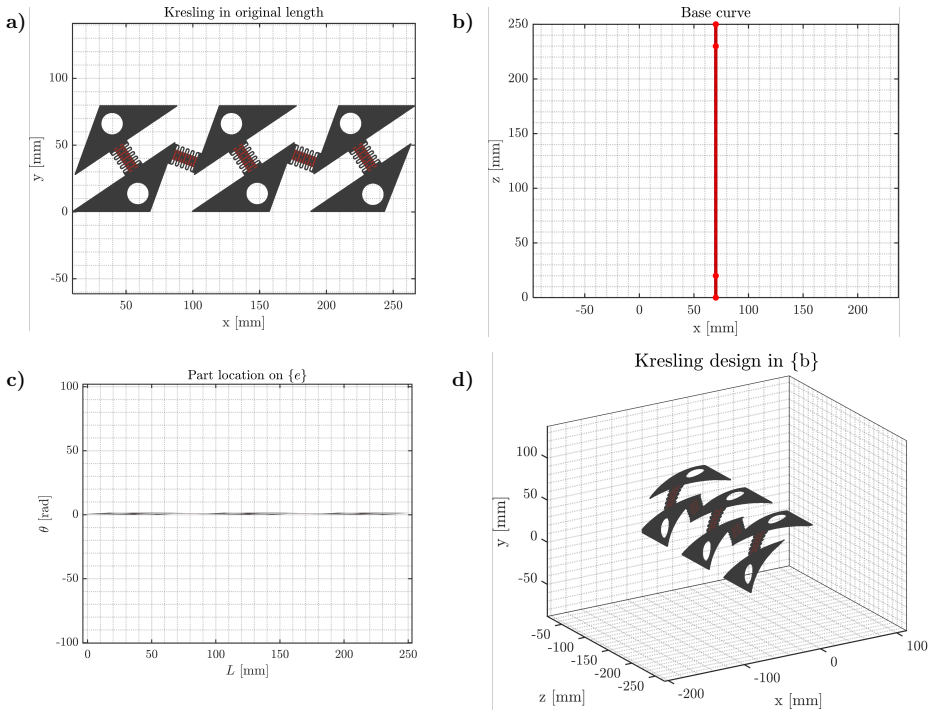

Figure 6.31: Design process of a Kresling pattern on a Cylindrical-shaped build platform. a) Original part in $\{b\}$. b) Build platform used to define $\{e\}$. c) Deformed and located part to fit in $\{e\}$. d) Final design result in $\{b\}$

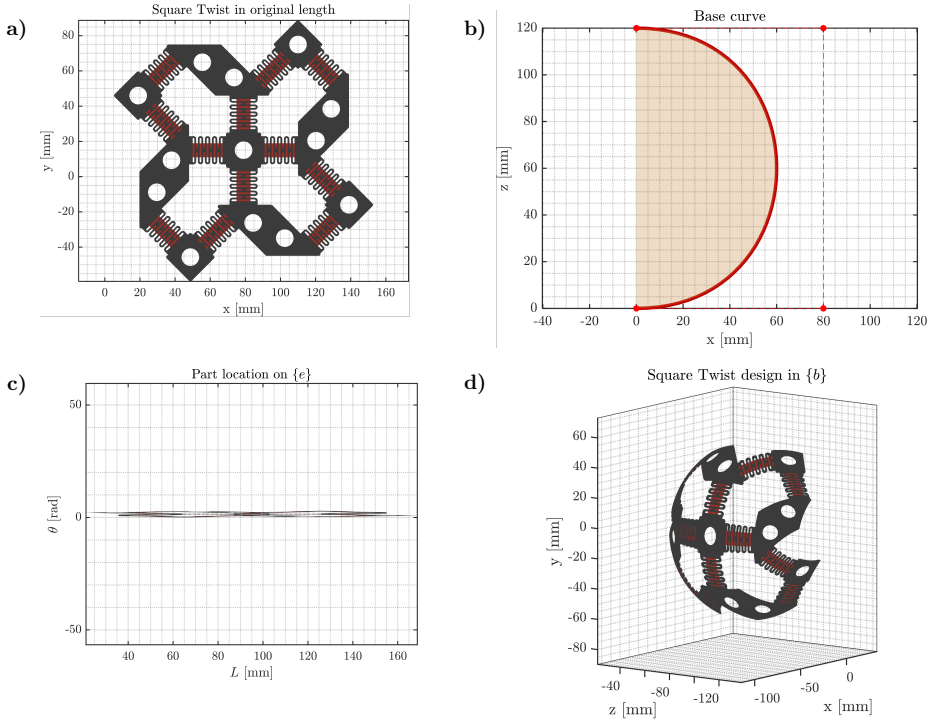

Figure 6.32: Design process of a Square Twist pattern on a Spherical-shaped build platform. a) Original part in $\{b\}$. b) Build platform used to define $\{e\}$. c) Deformed and located part to fit in $\{e\}$. d) Final design result in $\{b\}$

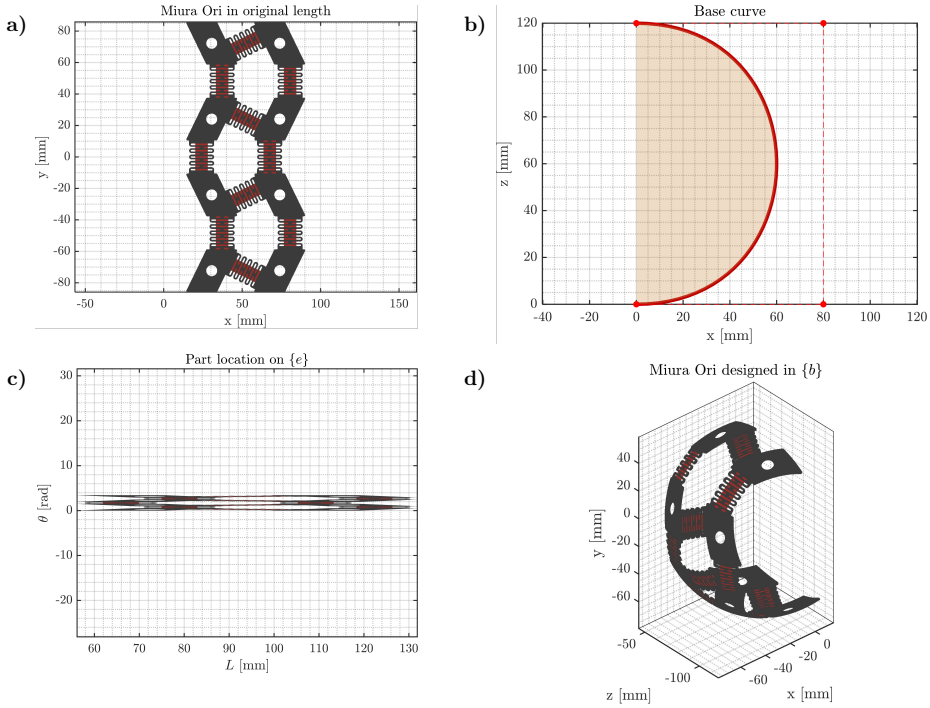

Figure 6.33: Design process of a Miura Ori pattern on a Spherical-shaped build platform. a) Original part in $\{b\}$. b) Build platform used to define $\{e\}$. c) Deformed and located part to fit in $\{e\}$. d) Final design result in $\{b\}$

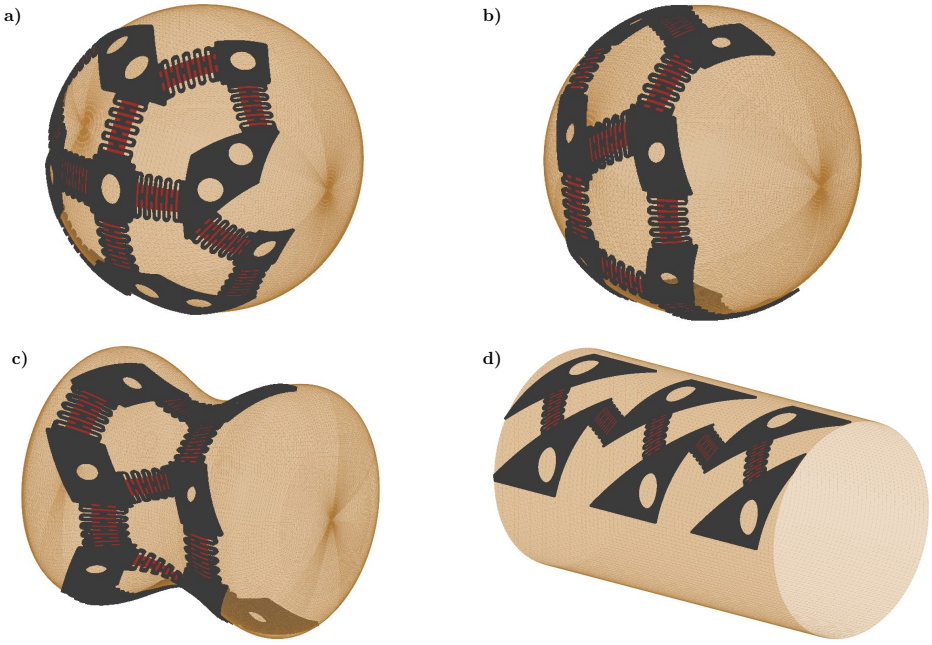

Figure 6.34: DfNPAM patterns presented on their built platform. a) Square Twist on spherical build platform. b) Miura Ori on spherical build platform. c) Miura Ori on double curvature build platform. d) Kresling on a cylindrical platform.

Chapter 7

Applications of Robot-Based Non-Planar Additive Manufacturing

This chapter is based on the methodology developed and validated in Chapter 4, applied to case studies in bioengineering. Two in-depth studies have been conducted: the construction of coronary stents and the use of origami patterns for designing skin expansion devices. In both cases, the objective is to highlight the advantages of this new non-planar layer-based slicing methodology over traditional slicing mechanisms.

The process is divided into an analysis of the case study, starting with the STL model of the part to be manufactured. From there, the mechanical requirements are evaluated, followed by an examination of the build platform, printability (including the feasibility of part removal and support structures), trajectory generation, and exporting the trajectory file for implementation in the robotic manipulator.

7.1 Coronary stents

Coronary stents are essential medical devices used to treat coronary artery disease by keeping vessels open after angioplasty. Enhancing their mechanical strength is critical to ensure long-term durability, reduce the risk of complications like restenosis and stent fracture, and improve patient outcomes. This section explores key elements of coronary stent design, emphasizing shape optimization, the mechanical forces at play, and current design approaches.

The geometry of a stent plays a crucial role in determining its mechanical performance, flexibility, and interaction with arterial walls [202]. Common stent geometries include:

- **Mesh structures:** These stents are typically composed of interconnected struts arranged in patterns such as:
  - Hexagonal patterns: Offering a balance of radial strength and flexibility.
  - Zigzag or spiral patterns: Designed to improve flexibility and conform to the natural curvature of the vessel.

- **Helical designs:** These stents imitate the natural helical structure of arteries, providing enhanced flexibility and reducing the risk of vessel trauma.
- **Tapered geometries:** Featuring gradually changing diameters along the stent, they adapt to varying vessel sizes, minimizing stress concentrations.
- **Lattice and honeycomb structures:** Engineered to optimize material use while maintaining high strength and flexibility.

Enhancing the mechanical resistance of coronary stents requires a combination of material science, mechanical engineering, and bioengineering principles. The selection of materials is critical, with common choices including cobalt-chromium alloys for their superior strength and radiopacity, nitinol for its exceptional flexibility and shape-memory properties, and titanium alloys for their biocompatibility and corrosion resistance. Each of these materials contributes to the stent's ability to withstand the mechanical demands of the cardiovascular environment while ensuring patient safety [203].

In addition to material selection, optimizing the stent's geometry plays a vital role in improving mechanical performance. Computational techniques like topology optimization help design stent structures that maximize strength and durability with minimal material usage, leading to innovative geometric patterns that traditional methods may overlook. Finite Element Analysis (FEA) is often employed to simulate the stent's behavior under various mechanical loads, identifying stress concentrations and potential failure points to inform design improvements. Manufacturing techniques such as laser cutting, 3D printing, and additive manufacturing are essential to producing complex stent geometries, which, combined with multifunctional designs like drug delivery mechanisms, further enhance mechanical resistance without compromising functionality.

From the aforementioned materials, titanium alloys are the most commonly 3D printed using electron beam technologies (EBM). Titanium alloys, particularly Ti-6Al-4V, are well-suited for electron beam melting due to their high melting point, biocompatibility, and strong mechanical properties, making them ideal for medical applications like stents and implants [202].

Designing stents to enhance mechanical resistance presents several key challenges, with the primary focus being to improve radial strength while minimizing material usage. Achieving this balance requires innovative design approaches, such as optimizing the geometry of stents to reinforce areas subjected to high stress. A well-designed stent must withstand significant pressure while maintaining a lightweight structure, ensuring it can effectively support the artery without increasing the risk of complications. This challenge becomes particularly complex when considering the need to optimize strut thickness and distribution to prevent material fatigue or failure under constant stress [79].

Another significant challenge in stent design is improving fatigue resistance, especially for self-expanding stents made from materials like nitinol. These stents must endure repeated cyclic loading as the artery moves and expands, making resistance to fatigue crucial in preventing fractures over time. Designers must carefully balance flexibility and strength, fine-tuning parameters like helical patterns to improve durability without compromising the

stent's ability to conform to the vessel's natural shape. Ensuring long-term performance while maintaining structural integrity is essential in preventing restenosis and ensuring the overall success of the stent [204].

7.1.1 Case Study description

After identifying the challenges related to the design, manufacturing, materials, and use of coronary stents in medical applications, a non-planar additive manufacturing methodology is proposed for stent production. This approach incorporates various mesh structures to reduce fatigue damage compared to traditional flat-layer manufacturing techniques.

The case study is subdivided into three sections. The first section outlines the guidelines for selecting the shape of the layer and its definition, the second section focuses on the trajectory generation algorithm employed for slicing the design in stereolythography format (STL) and the final section focuses on the use of the methodology to create a build platform that meets the requirements for morphology and extraction capability of the manufactured part.

Build platform definition in $\{b\}$

The stent geometry selected for optimization is shown in Figure 7.1 where the reference frame of the STL points is represented. The goal is to minimize fatigue damage by stacking layers in a direction that reduces the staircase effect. The non-planar layers are designed to be perpendicular to the surface defined by the stent's inner structure. This approach not only addresses fatigue damage but also meets the radial force resistance requirements. Both critical performance metrics are significantly improved compared to the traditional methodology, where layers are stacked in the figure's xy-plane.

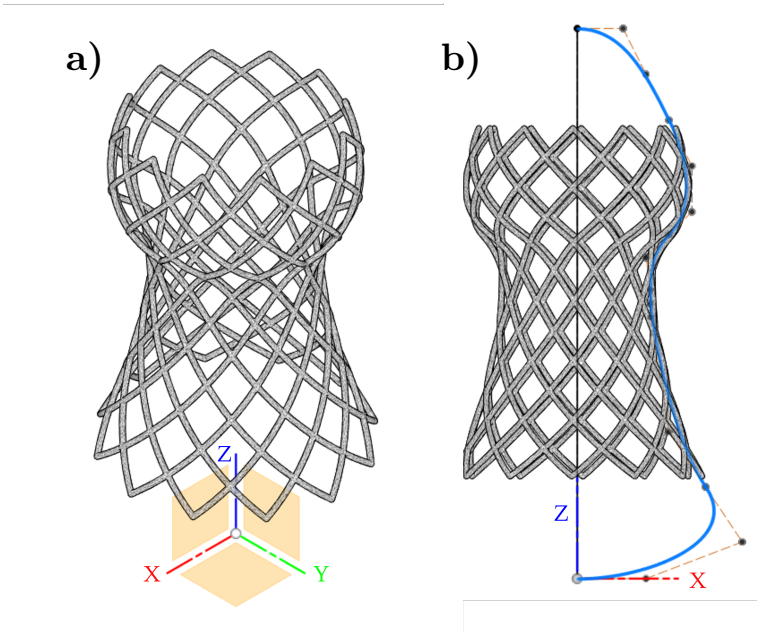

Figure 7.1: s) Stent's $\{model\}$ reference system with the Z axis as the axis of symmetry. b) Revolution build plate control polygon referred to the xz-plane.

After selecting the axisymmetric layer stacking direction, it is essential to parametrically define a generatrix curve Γ. This curve outlines the surface of revolution that will shape the build platform. In this case, the platform takes on an hourglass form, with its parametric definition, as the control polygon of 16 points, detailed in Table 7.1. These points define parametrically the generatrix showed on Figure 7.1.b.

Table 7.1: Parametric build platform's generatrix curve, Γ, defined in the xz-plane

Point Reference	**X[mm]**	**Z[mm]**
1	0	0
2	7.5	0
3	18	4
4	14	10
5	10	16
6	8	28.5
7	8	30
8	8	31.5
9	7.5	35
10	10	37.5
11	12.5	40
12	12.5	45
13	10	50
14	7.5	55
15	5	60
16	0	60

Once the generatrix of the base plate has been formally defined, it is essential to verify that it satisfies the necessary conditions for the transformation between $\{b\}$ and $\{e\}$ to occur within the geometry's domain. The generatrix must be at least G^1 continuous throughout its parameter domain, without any cusps or nodes. Additionally, bijectivity must be ensured within the geometry's domain, while bijectivity outside this domain is irrelevant.

In our case, Figure 7.2 demonstrates that, due to the low curvature of the build platform in its central region, bijectivity is correctly maintained within the stent's geometric domain. However, points outside the green shaded area in the figure can be approached perpendicularly from two or more different directions (blue lines). As shown, the entire axisymmetric part of the stent to be printed lies within the green area, making it possible to laminate using the proposed algorithm. Furthermore, the stent thickness could be increased while still maintaining compatibility with the build platform.

The build platform is defined by rotating the generatrix around the z-axis of the frame $\{model\}$ as shown in Figure 7.3. The successive layers will be stacked normal to this surface at each point generating the final solid with conformal layers.

The proposed layer stacking system concentrates the staircase effect at the upper and lower ends of the stent, leaving the entire central surface free of it in the radial direction. In this

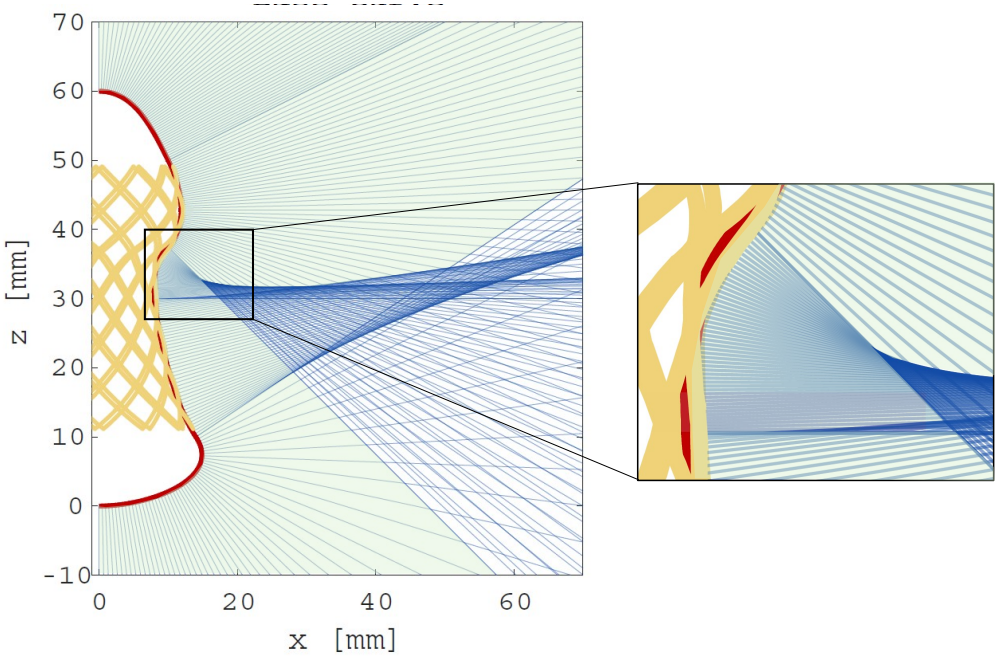

Figure 7.2: Printable area associated to the proposed build plate defines as the green surface.

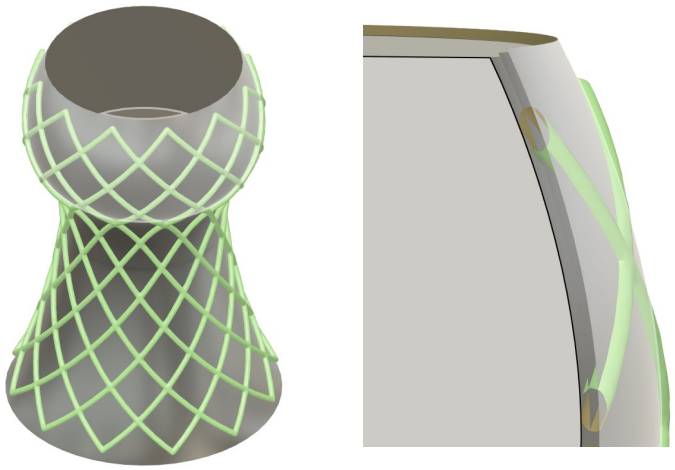

Figure 7.3: Complete build plate and slicing surfaces representation for the defined generatrix.

same direction, the stent's the mesh operates under compression and expansion along the defined print lines, aiming to reinforce the two initially considered effects.

Trajectory generation in {e}

Once the cutting surfaces for the stent to be laminated in the case study are selected, the corresponding trajectories are generated. Trajectory generation on curved surfaces is highly complex, as it requires not only defining the waypoints' positions $(X, Y, Z)_{\{b\}}$, but also ensuring the nozzle's orientation remains perpendicular to the lamination surface. This is where the definition of space $\{e\}$ offers its greatest advantage. In this transformed subspace, the layers

are always flat, and the normal vector to the surface is $\{0, 0, 1\}_{\{e\}}$ at every point. Leveraging this property, trajectories can be generated using commercial software like CURA and then transformed back into the original Cartesian subspace, with both position and orientation accurately defined.

In this particular case, the lamination of the transformed part in space $\{e\}$ was carried out using the commercial software Ultimaker CURA. The complexity of the part in this subspace made it challenging for the custom algorithm to generate flat trajectories accurately. However, since the part consists solely of walls without any infill, the lamination was successfully completed using this method.

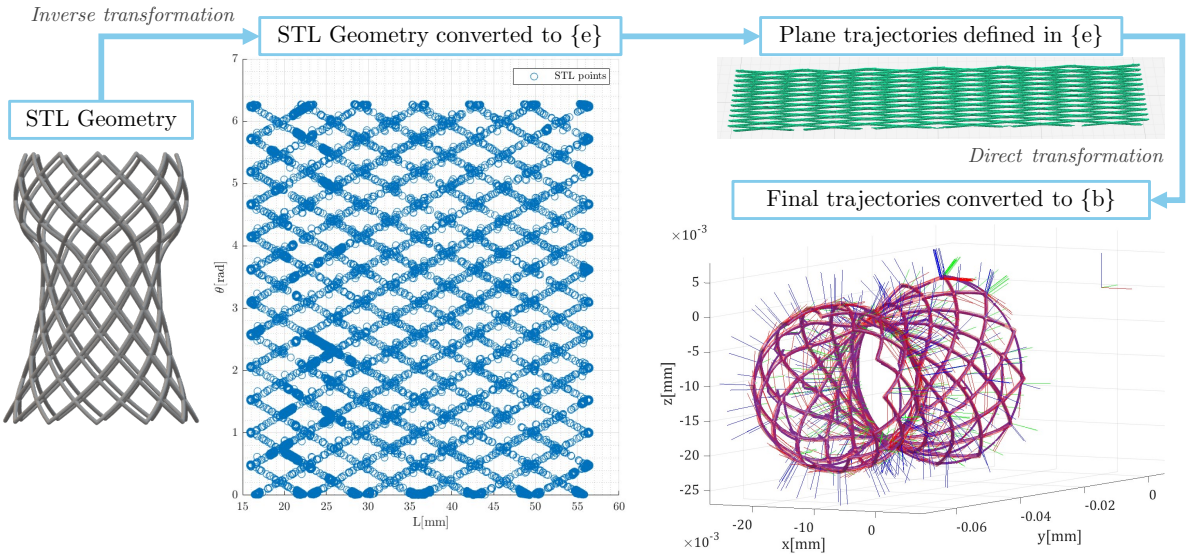

Figure 7.4: Complete slicing process. The points and connectivity matrices defined in the STL geometry in $\{b\}$ are transformed to $\{e\}$. Once transformed the new geomtry is sliced. The generated trajectories are then transformed into $\{b\}$ obtaining the final toolpath (both points and tool orientation).

The procedure is illustrated in Figure 7.4. Starting from the original stent design in $\{b\}$, and using the control polygon and layer definitions from Table 7.1, the STL file of the stent is transformed into the subspace $\{e\}$ via the inverse transformation outlined in 5.8, where it becomes a planar shape. Once in $\{e\}$, the STL file is imported into a commercial solid lamination software, in this case, Ultimaker Cura, to generate the G-code typically used by conventional 3D printers. In our case, since a robotic manipulator is used for additive manufacturing, each point and orientation defined in the G-code is extracted and transformed back into subspace $\{b\}$ using the direct transformation defined in 5.11. After validating for potential interferences and singularities, this code is used to command the robot to fabricate the part using additive manufacturing.

The trajectories extracted from Ultimaker Cura in $\{e\}$ must be pre-processed before applying the direct transformation and returning them to $\{b\}$. This processing includes classifying the trajectories based on their type, as well as incorporating additional points to avoid the chordal error that may arise due to the bed's curvature.

Built platform definition preparation

Once the trajectories for the robotic manipulator have been defined, the build platform on which the stent will be formed is designed. Due to the stent's complex curvature, it would be impossible to extract it from the build platform that generates the slicing surfaces defined in Table 7.1. To address this, the methodology outlined earlier is applied to develop a support structure that will later be removed, allowing the stent to be built on a cylindrical platform.

The proposed support structure is made from an easily removable material, such as polyvinyl acetate (PVA), though other materials can also be used as long as they are laminated and can be easily detached after printing is completed.

Both the support structure and the stent are fabricated simultaneously on a base piece referenced to the robot's Tool Center Point (TCP). The complete setup, including the aluminum build plate and its coupling to the robot, is shown in Figure 7.5.

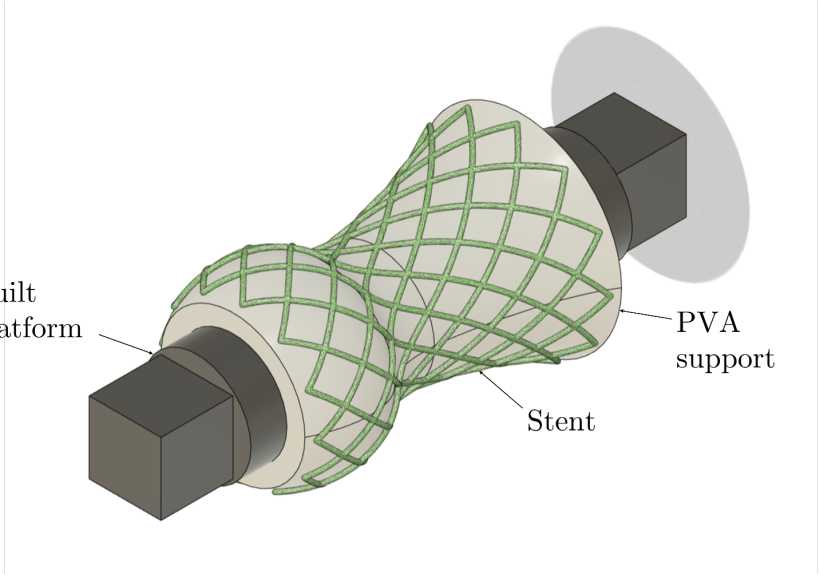

Figure 7.5: Manufacturing set up consisting of built platform, PVA support and stent. THe model has been adapted to be printed on the real built platform in Figure 5.27.

7.1.2 Results and discussion

The primary outcome of this work is the successful generation of trajectories in $\{b\}$, defined by both position and orientation, with normal vectors aligned to the surface of a coronary stent. The stent is constructed with layers normal to its inner surface. Figure 7.6 illustrates the first of these layers, with the normal direction indicated at each point. Due to the complexity of these trajectories, it was essential to evaluate the feasibility of their execution beforehand. For build platforms with low curvature, robot collisions are easily avoidable, and optimal robot positioning can mitigate the risk of encountering singularities during printing. This method of lamination shows promise for enabling the printing of various grid structures in stents, as demonstrated in Figure 7.7.

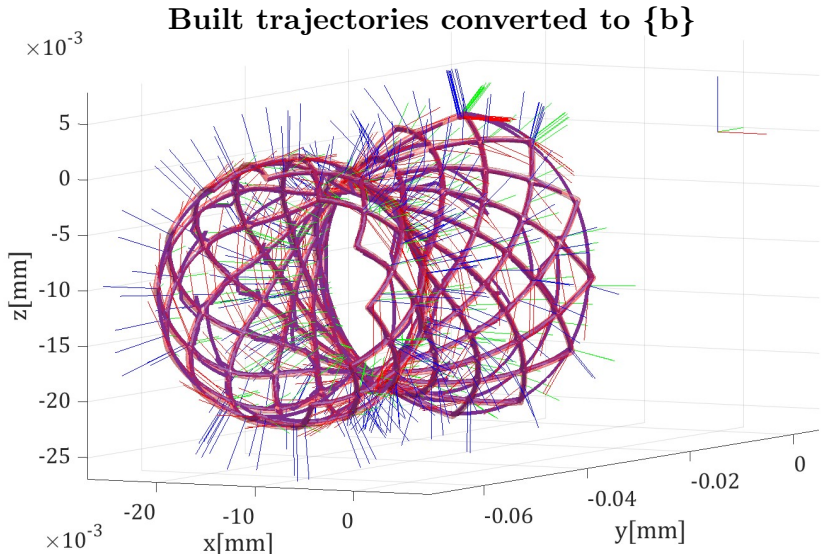

Figure 7.6: Stent's robot based NPAM trajectories defined in $\{e\}$. Slicing surface normal vectors on each waypoint shown in blue. For clarity, only the first layer has been represented.

A significant secondary contribution of this methodology is the design of the printing support. In this case, the support was made from Polyvinyl Acetate (PVA) to allow the stent to be generated on a cylindrical bed attached to the robot. The support structure was printed on a cylindrical slicing surface, as shown in Figure 7.8. While a soluble PVA support was used for convenience, the curved lamination process facilitated by this methodology is flexible enough to allow for any support geometry, with customizable filler densities and shapes, depending on the part's requirements.

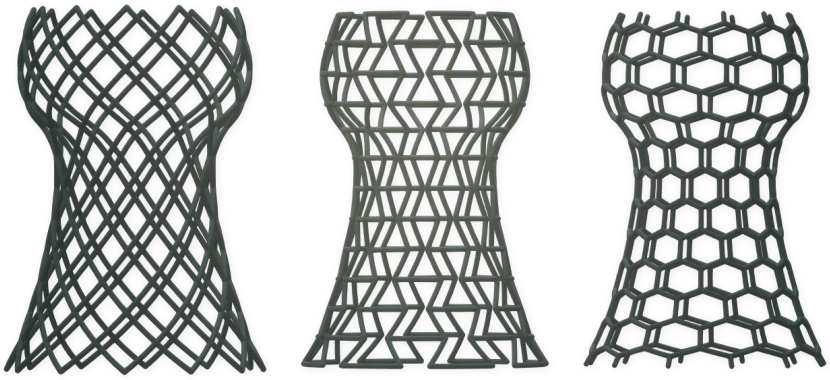

Figure 7.7: Examples of different grids applied to the stent shape and build platform proposed in this case study.

The analysis of the generated trajectories and the application of the curved lamination technique also revealed improvements in the precision and quality of the layers. By aligning each layer perpendicularly to the stent's inner surface, we achieved a more uniform distribution of forces, which contributes to enhanced structural integrity. Moreover, the versatility of this approach opens up the potential for fabricating more complex geometries that were previously

challenging to produce with traditional planar slicing methods. This demonstrates the broader applicability of this methodology to other medical devices and mechanical structures that require fine-tuned lamination strategies.

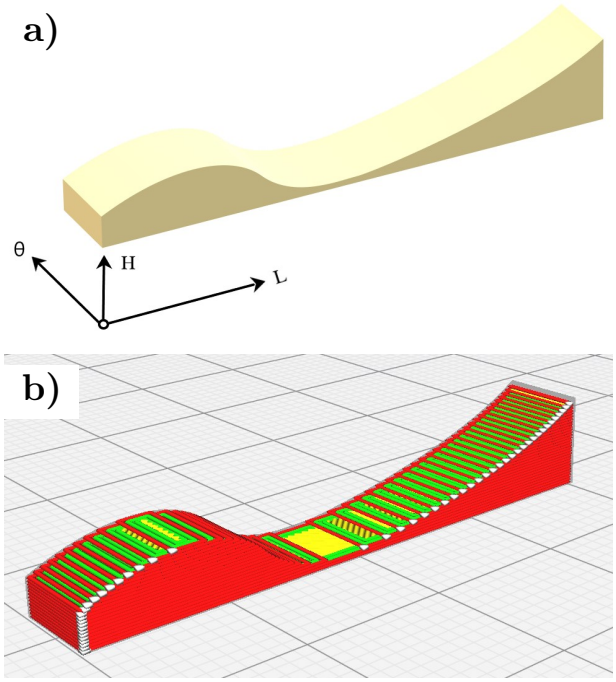

Figure 7.8: a) PVA Support defined in Figure 7.5 transformed to $\{e\}$. b) Plane trajectories defined by the slicer in $\{e\}$.

The main contribution of this article is the achievement of coronary stent trajectory planning by robot-based NPAM. This non-planar slicing method is intended to improve the mechanical properties and surface finish of the stent. For this purpose, the versatility of the developed methodology has been demonstrated in terms of the selection of the slicing surface based on axysymmetric generatrices. In addition, the slicing methodology has been used to generate the structural supports of the lamination and to facilitate its extraction from the build plate. Finally, different types of stet grids that could be printed on the same base have also been considered.

The main limitation of the use of the slicing method in other case studies is associated with the identification of the bijective area defined by the generatrix curve where the entire geometry must be located. Once this limitation is overcome, it will be the limits established by the robot used, manipulability and singularities, which will set the limit for the use of this methodology. Finally, the geometries need to be manufactured to test their mechanical behaviour improvement.

7.2 Design of an origami-type robotic gripper

7.2.1 Case study description

Soft robotic grippers, especially those inspired by origami designs, represent a rapidly growing field at the intersection of materials science, robotics, and biomechanics. These systems aim to mimic the dexterity and adaptability of biological organisms, providing superior performance in delicate tasks such as handling fragile objects or operating in unpredictable environments. The foundation of this field is the development of compliant, flexible materials and actuation systems, enabling grippers to conform to objects of various shapes, sizes, and fragilities [205, 206].

Soft robotic grippers rely heavily on elastomeric and flexible materials that allow for reversible deformation. Initial research focused on materials such as silicones, hydrogels, and polyurethane, which are known for their stretchability and compliance. These materials are often paired with pneumatic, hydraulic, or electrical actuation systems, enabling smooth movement without requiring rigid components. The selection of materials plays a crucial role in determining the durability, strength, and precision with which the grippers can handle a variety of objects, making it essential to choose materials that balance flexibility with mechanical resilience [207, 208].

Origami-inspired mechanisms enhance the gripping efficiency of soft robots, enabling compact storage when inactive and expansion into various shapes that conform to different objects. This adaptability makes origami an ideal design strategy for applications requiring precision and versatility in soft robotics [209].

In this context, the methodology is used to design and fabricate a flexible robotic gripper. This design, based on foldable origami-like structures, leverages the non-planar slicing capability to create mechanisms that can adapt to complex shapes and tasks. By applying the Slicing space, the geometry of the gripper is designed in a 2D space, which is then transformed into a functional three-dimensional structure with optimized flexibility and addapted to the grasped object. The workflow of the case study and the design parameters are shown in Figure 7.9.

For the purposes of this case study, a Yoshimura-style origami design has been selected as the base design. This origami pattern is well-known as a design possibility for a gripper [209], and it has been proven to be planarly printable through multi-material MEX techniques by combining rigid PLA zones (black) and flexible TPU-95 zones (red), as shown in Figure 7.10.

In this flat test, the behavior of flexible joints with various TPU printing directions has been validated, resulting in a functional flat design with an open resting state. The goal is to employ non-planar printing to replicate this case study in non-planar additive manufacturing, achieving the same structural results but with a normally closed resting state. This way, the robotic gripper can hold an object when no force is applied to it.

When applying this design method, it is critical to properly locate the part within this $L\theta$-plane, both in position and orientation, to ensure the desired results. For this case study, the centroid of the mechanism was located in the middle of the build platform, so that $L_{centroid} = L_{curve}/2$ for all cases presented. Another consideration of note is that θ is an

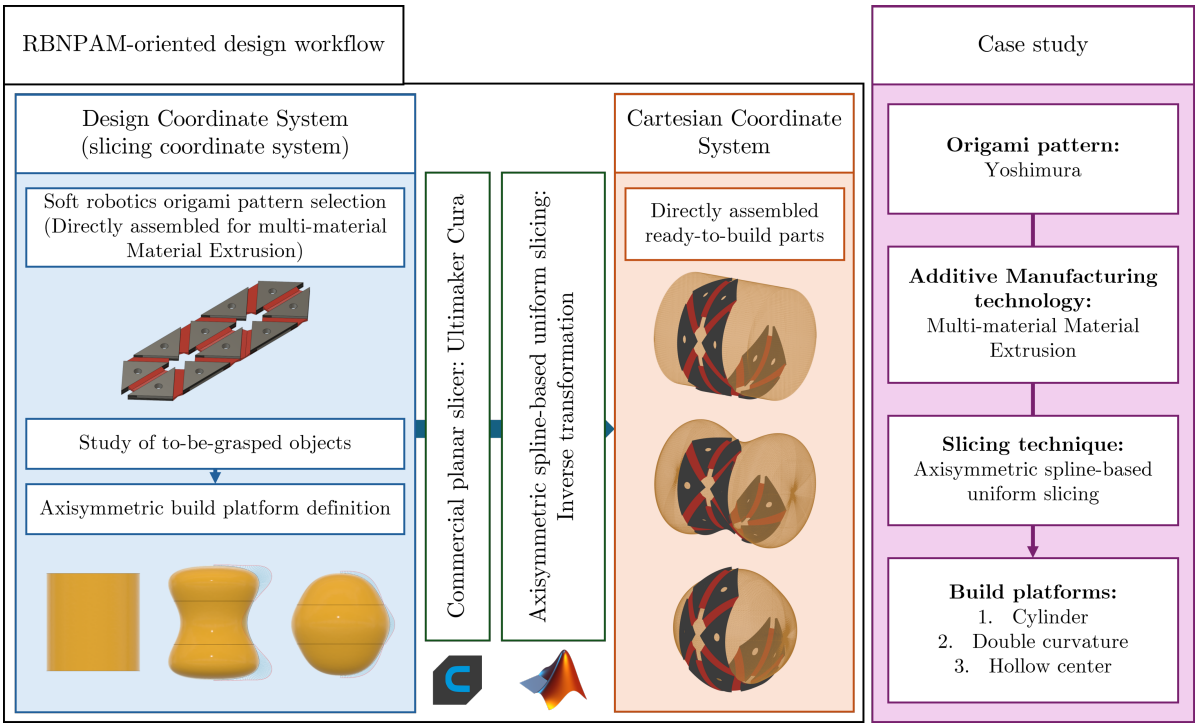

Figure 7.9: Left-hand side: design workflow for multi-material RBNPAM soft robotics grippers. Right-hand side: selected parameters for the present case study.

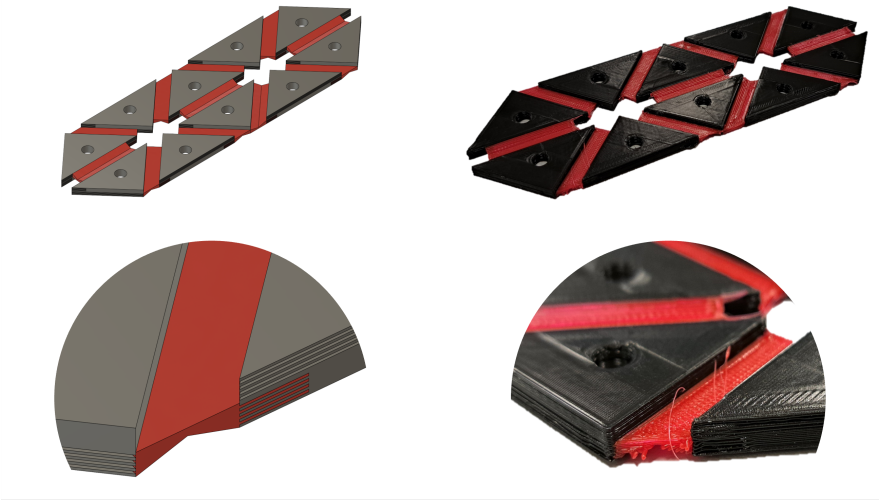

Figure 7.10: Example of the Yoshimura origami design proposed for the present case study. On the top side, CAD design and in-house manufactured prototype by multi-material MEX. On the bottom side, a detail of the interlocking between the stiff material (poly-(lactic acid), in black) and the compliant material (thermoplastic polyurethane 95A, in red).

angular measurement, ranging from 0 to 2π radians. Designers must scale their mechanisms accordingly. For this case study, a θ range of $[0, 3\pi/2]$ was selected to create sensible designs. Lastly, the parts shall not have any non-positive H coordinate, as this would imply a collision between the build platform ($H = 0$) and the extruder head in the actual manufacturing process. These considerations are added to the previously mentioned limitations, which depend on the generatrix curve used.

$\{b\}$ as a functionality-oriented Design Space

Regarding the functionality aspects belonging to $\{c\}$, designers must firstly understand the graspable geometric entities of the parts of interest. This geometry (usually the part exterior) defines the build platform. For the present case study, three different build platform geometries are defined to fully showcase the design possibilities: a cylindrical build platform for tubular objects (cylinder case), an hourglass-shaped build platform for objects with handle-like geometries (double-curvature case), and a quasi-spherical build platform for convex objects (hollow case). These build platforms are defined through composite Bézier splines, and their control polygons are described in Table 7.2.

Table 7.2: Definition of composite Bézier splines for build platforms

Control polygons definition					
Cylinder		**Double curvature**		**Hollow**	
$\boldsymbol{x}$ **[mm]**	$\boldsymbol{z}$ **[mm]**	$\boldsymbol{x}$ **[mm]**	$\boldsymbol{z}$ **[mm]**	$\boldsymbol{x}$ **[mm]**	$\boldsymbol{z}$ **[mm]**
48	100	0	100	0	100
48	100	48	100	27.5	100
48	84	42.5	84	35	84
48	69	35	69	42.5	69
48	69	35	69	42.5	69
48	54	27.5	54	50	54
48	46	27.5	46	50	46
48	31	35	31	42.5	31
48	31	35	31	42.5	31
48	16	42.5	16	35	16
48	0	48	0	27.5	0
48	0	0	0	0	0

All these geometries pose a question in terms of reachability, both from a process and mathematical perspective. Regarding process reachability, the dimensions and curvature of the build platform may make it impossible for the robotized station to calculate a proper pose through inverse kinematics. Additionally, the extruder nozzle semi-angle must be compatible with the build platform curvature to avoid collisions. These aspects will be addressed in future works. More interestingly, from a mathematical perspective, the build platform geometry limits the printable regions due to the characteristics of the isomorphism, especially in areas with negative curvature as has been explained before.

For this case study, bijection check is performed for the double curvature case, as the other two build platforms are convex.

RBNPAM trajectory generation

Once the compliant mechanism has been designed and the build platform has been selected, the commercial software Ultimaker CURA was used for generating $\{e\}$-based toolpaths in this case due to the complexity of the model, which required many hours of computation. When using commercial software, it is necessary to make adjustments to the reference system in which the toolpaths are generated and to pay special attention when referencing them back to the $\{b\}$ system once they are converted to the World space. Then, utilizing the direct transformation, it is possible to map these trajectories onto $\{b\}$ by means of parsing the resulting G-code. Of note, it may be necessary to interpolate the parse data to account for the model scale in the θ direction and obtain smoother paths. This is critical in the success of inverse kinematics algorithms applied to these $\{b\}$ paths when implementing them in an actual robotized station.

7.2.2 Results and discussion

This section presents and discusses the results obtained from the case study on the design and planning of an origami-based robotic gripper. The presentation of results is divided into the generation of the CAD file, the outcomes of verifying the bijectivity conditions in cases of negative curvatures, the final design results, and, finally, the printing trajectories.

CAD model preparation

As explained along the methodology, the compliant mechanism CAD model shall undergo several transformations. This includes the preparation of the CAD model itself, scaling the θ coordinate according to the designer's choice, and properly locating the part within the $L\theta$-plane. Examples of these transformations are shown in Fig. 7.11.

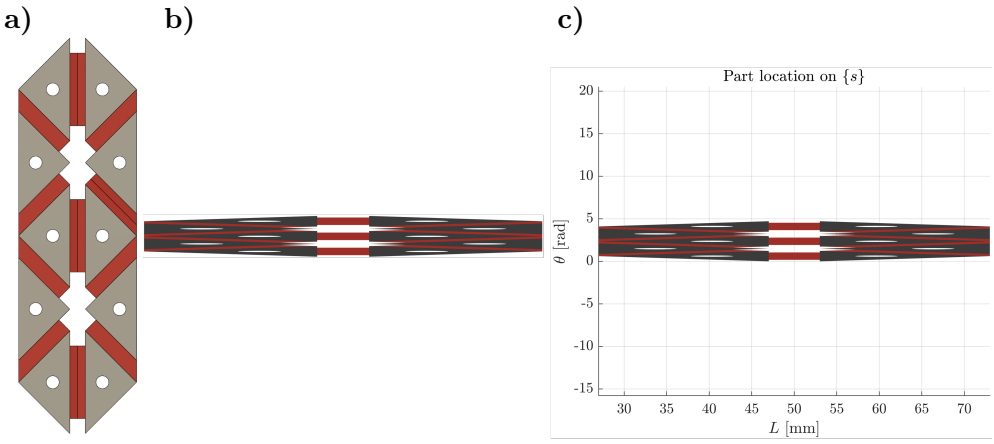

Figure 7.11: a) CAD model of the compliant mechanism based on a Yoshimura-based origami pattern. b) Model after θ-scaling. c) Model positioned in $\{s\}$ with $L_{centroid} = L_{curve}/2$.

The figure illustrates the initial design of the flat CAD model, where the components of the Yoshimura origami structure are assembled using various materials. Once the assembly is validated, it is scaled to fit within the Design space. Following this, the piece is positioned in the LTheta plane, where the desired transformation location is selected. The final model will encompass 5 radians of circumference in the $\theta-$direction and will measure $50[mm]$ in the $L-$direction.

Double curvature build platform bijection check

The selection of negative curvature build platforms may result in either inaccessible areas in terms of numerical resolution or regions with a multiplicity of solutions. For a part to be manufactured through this methodology, all model points shall be contained within the same isomorphism region. This can be visually checked for the double curvature case, as can be seen in Figure 7.12.

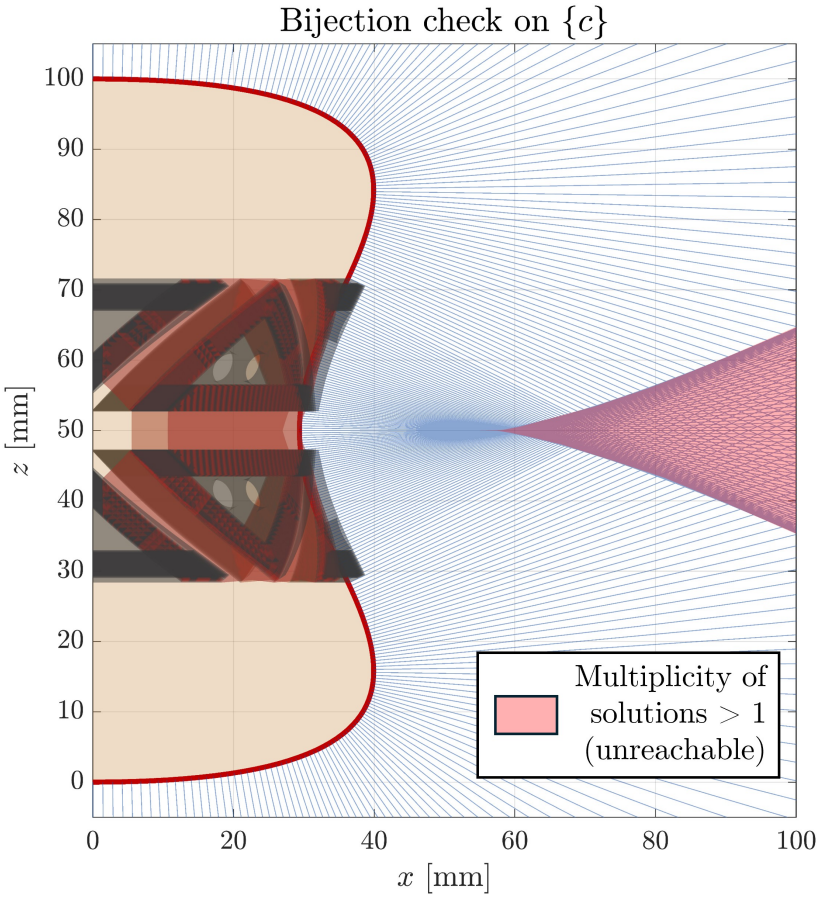

Figure 7.12: Representation of the build platform (in yellow shade), with the Cartesian part located on it. The red shaded areas indicate the unreachable areas, in this case, with a multiplicity of homomorphisms greater than 1, whereas the blue-striped areas show the reachable region.

World space models and RBNPAM path planning

Once the methodology has been applied for all three build platforms proposed, the actual